

DESIGN AND VALIDATION OF AUTONOMOUS RAPID MAPPING SYSTEM
USING SMALL UAV

By

WILLIAM SCOTT BOWMAN

A THESIS PRESENTED TO THE GRADUATE SCHOOL
OF THE UNIVERSITY OF FLORIDA IN PARTIAL FULFILLMENT
OF THE REQUIREMENTS FOR THE DEGREE OF
MASTER OF SCIENCE

UNIVERSITY OF FLORIDA

2008

© 2008 William Scott Bowman

To Mom, Dad, Michael and Kelley.

ACKNOWLEDGMENTS

First and foremost, I would like to thank my immediate and extended family for their unwavering support throughout my academic efforts. I would like to thank Grandma Thoenes for her gracious generosity and involvement in my life; I wish I could tell Grandpa Thoenes how influential his love for engineering has been on me. It too has become my passion. I would like to thank Grandpa Bowman for providing me with my obvious entrepreneurial spirit and strong work ethic. I extend my greatest appreciation to the Lee family for being so supportive of me. I look forward to joining your family.

I would like to thank Dr. Peter Ifju for providing me with the means to grow academically. I have always heeded your advice and have appreciated your approachable personality. I thank Dr. Franklin Percival for being such a great mentor and friend. I have enjoyed the collaboration among sciences; we have achieved something great. I thank Dr. Mohamed for providing his expertise in Geomatics and Inertial Navigation; it has inspired my work here. Additionally, I thank Kyuho Lee for being a great leader in the MAV Lab. I have enjoyed learning from you.

I thank my friends for being there when I needed them. I especially thank Adam and Mike for their help and humorous nature on this project. You guys have been great to work with. I will miss “junk-works”. I would also like to thank Baron for being such a great colleague and friend through grad school. Thanks again to my friends, Larry Taylor and John Lane of the C.O.E. for their support. Thanks again to Kelley for all her editing and word processing skills!

I would like to give my goodbyes to the University of Florida. I was given the absolute best “college experience”. There is no other college in the country that can provide all there is to offer here; stellar academics and three national championships. GO GATORS!!

Finally, I would like to thank Rusty, the tabby cat, for providing me with comforting companionship during the best and worst times in the writing of this thesis.

TABLE OF CONTENTS

	<u>page</u>
ACKNOWLEDGMENTS	4
LIST OF TABLES	7
LIST OF FIGURES	8
LIST OF ABBREVIATIONS.....	11
ABSTRACT.....	13
CHAPTER	
1 INTRODUCTION	15
Motivation.....	15
The Polaris UAV Overview.....	17
Georeferencing and Rapid Mapping.....	18
2 LITERATURE REVIEW	20
Small Unmanned Aerial Vehicles	20
Aerial Imaging and Georeferencing	21
Digital Mapping.....	23
3 POLARIS UAV AIRFRAME.....	25
Construction.....	25
Assembly	27
4 POLARIS UAV ELECTRONICS.....	34
Motor Selection and Controller	34
Actuators.....	35
Autopilot.....	35
Global Positioning System Receiver	36
Subsystem Control Hardware	37
Data Storage.....	39
Cameras	39
Polaris Power Management.....	41
Ground Control Station.....	43

5	POLARIS UAV SOFTWARE	51
	Firmware.....	51
	Graphical User Interfaces	52
	Camera Synchronization.....	53
6	CAMERA CALIBRATION AND INITIALIZATION.....	58
	Calibration Software.....	58
	Initialization Jig.....	62
7	RAPID MAPPING	68
	Coordinate Frames.....	68
	Direct Georeferencing	71
	Direct Linear Transformation Method.....	74
	Photo Geo-Registration	76
	PolarisView Graphical User Interface.....	77
9	MAPPING OUTPUT AND ANALYSIS	84
	Data Set.....	84
	Results.....	85
10	SUMMARY, CONCLUSION AND RECOMMENDATIONS FOR FUTURE WORK..	100
	Summary.....	100
	Conclusion.....	100
	Recommendations for Future Work	101
	Georeferencing	102
	Small Unmanned Aerial Vehicle Control.....	104
APPENDIX		
A	POLARIS VIEW GENERATED DATASET	106
B	DEVICE PARAMETERS	110
LIST OF REFERENCES.....		111
BIOGRAPHICAL SKETCH		115

LIST OF TABLES

<u>Table</u>	<u>page</u>
3-1 Wing and stabilizer design parameters	30
4-1 Root-mean-square errors in the Kestrel v2.2 INS/GPS in near level conditions.....	45
7-1 The WGS84 reference ellipsoid values.....	79
8-1 Indicates calculated boresight misalignments for the data set.....	88
A-1 Compensated_Pic_Data file used for rectification, area assessment and mapping in the results section.....	107
A-2 Pertinent data entries for a given target. This data was used throughout the thesis.	108
B-1 Autopilot Sensor Parameters.....	110
B-2 Canon A650 IS Parameters.....	110

LIST OF FIGURES

<u>Figure</u>	<u>page</u>
3-1 Unpainted Kevlar [®] Fuselage used for the Polaris UAV	30
3-2 Polaris' wing, horizontal and vertical stabilizer plan forms	30
3-3 Tensioning acetate film over fiberglass skinning creating a smooth external surface.	31
3-4 Process for compressing fiberglass curing epoxy to EPS foam wing cores	31
3-5 Saddle hatch for programming access of PDIB processor and wing connectivity	32
3-6 Horizontal stabilizer tail boom mounting hardware	32
3-7 Completed Polaris UAV airframe A) Bird's eye view B) side view	32
3-8 Airboat launch and recovery setup.	33
3-9 Polaris day and low-light flying configuration	33
4-1 Procerus [®] Autopilot - Kestrel v2.2	45
4-2 One Watt Aerocom modem is mounted in tail to reduce EMI	45
4-3 Carbon fiber box for autopilot with waterproof interfacing electrical connectors	46
4-4 Elevator control loop.....	46
4-5 Throttle control loop	46
4-6 Aileron/Rudder control loop.....	47
4-7 Furuno GH81 GPS receiver on Polaris UAV	47
4-8 Custom designed "Power Distribution and Integration Board"	47
4-9 DostonChip SD Memory Card hardware used to store synchronized UAV orientation and location data	48
4-10 KX-141 CCD camera and installation location	48
4-11 One watt video transmitter (no antenna) and video control circuitry	48
4-12 Canon A650 Digital Camera payload.....	49
4-13 Unpopulated camera control board.....	49

4-14	Custom designed power module.....	49
4-15	Front and back of Ground Control Station (GCS).....	50
5-1	Atmega 128 MCU firmware flowchart.....	56
5-2	Virtual Cockpit software screen shot.....	56
5-3	PolarisLink software.....	57
5-4	Camera control window.....	57
6-1	Images used for camera calibration.....	64
6-2	Internal grid intersection points are based on square sizes and initial lens distortion coefficient k_c	64
6-3	Lens distortion model of Canon A650. A)Tangential lens distortion. B) Radial lens distortion.....	65
6-4	Complete lens distortion model.....	65
6-5	Comparison of distorted picture based on lens parameters. A) Original distorted picture B) Undistorted picture.....	66
6-6	Exterior camera parameters for indoor calibration.....	66
6-7	Field initializatoin process for determining camera boresight misalignment.....	67
7-1	Definition of coordinate frames used for direct georeferencing.....	79
7-2	Definition of Image Frame Coordinate System.....	80
7-3	Example of DLT projections from camera frame origin through image plane to ground coordinates in mapping frame satisfying collinearity conditions.....	80
7-4	Digitally Geo-registered Photos.....	81
7-5	PolarisView GUI software package.....	81
7-6	Offset menu in PolarisView for determining camera relative position and orientation....	82
7-7	Example of calibration image of taken just before survey flight.....	82
7-8	Example of area coverage assessment generated from PolarisView.....	83
8-1	Ground control targets used for spatial comparison in the mapping process.....	88
8-2	Polaris UAV flight route versus numeric target locations.....	88

8-3	Rectified images for data set are rectified and registered from PolarisView into Google Earth [®] 's interface	89
8-4	All pre-surveyed points were located in registered photos	89
8-5	Pre-survey location of the target versus measured values for those targets through the photos in Google Earth	90
8-6	UAV and camera attitudes at the time of commanded camera exposure	93
8-7	Residuals for all registered photos	94
8-8	RMS of Euclidean distances for all targets.....	97
8-9	Averaged combined pitch and roll effects on positional accuracy apparent in data.....	97
8-10	Simulated principal point error on the ground from IMU inaccuracies in pitch and roll.....	98
8-11	Rates of all UAV states during initial 20 photograph capture	98
8-12	Unaccounted for effects of an 87 millisecond synchronization error with high dynamics present.....	99

LIST OF ABBREVIATIONS

AC/DC	alternating current/direct current
ACK/NACK	acknowledge/no acknowledge
ADC	analog-to-digital
ASCII	American Standard Code for Information Interchange
CAD	computer-aided design
CCD	charge-coupled device
COTS	commercial off-the-shelf
DARPA	Defense Advanced Research Projects Agency
EMI	electromagnetic interference
EPS	expanded polystyrene foam
GCP	ground control point
GCS	ground control station
GIS	graphic information system
GPS/INS	global positioning system/inertial navigation system
GUI	graphical user interface
I/O	input/output
IMU	inertial measurement units
IP	internet protocol
KML	keyhole markup language
KV	rotations per minute per volt
LED	light emitting diode
LPP	leadless plastic package
mAH	milliampere-hour
MAV	micro air vehicle

MCU	microcontroller unit
MEMS	microelectromechanical systems
PCB	process controller board
PDIB	power-distribution-and-integration-board
PID	proportional-integral-derivative
PPS	pulse per second
PWM	pulse width modulation
RAM	random access memory
RISC	reduced instruction set computing
RISE	robust integral of the sign error
RMS	root-mean-square
SD	sandisk
SRAM	static random access memory
UAS	unmanned aerial systems
UAV	unmanned aerial vehicle
UF	University of Florida
USART	universal asynchronous receiver/transmitter
USB	universal serial bus
UTM	universal transverse mecaton
WAAS/DGPS	wide area augmentation system/differential global positioning system

Abstract of Thesis Presented to the Graduate School
of the University of Florida in Partial Fulfillment of the
Requirements for the Degree of Master of Science

DESIGN AND VALIDATION OF AUTONOMOUS RAPID MAPPING SYSTEM
USING SMALL UAV

By
William Scott Bowman

August 2008

Chair: Peter Ifju
Cochair: Ahmed Mohamed
Major: Mechanical Engineering

Advancements in inertial measurement, global positioning, and digital photography have allowed the development of small autonomous unmanned aerial vehicles (UAV) to be used for low altitude airborne imaging. The University of Florida has long been interested in using UAV's for wildlife and natural resource management. Digital, high resolution images taken from the UAV can be arranged to create a map of the flight coverage area. These maps can express a multitude of various environmental constituents that can be useful to biologists and ecologists alike.

Currently, aerial photography and mapping is generally done from a large fixed wing manned aircraft. Creating georeferenced maps from these photos is very expensive and time consuming, restricting the frequency in which the aerial photos are taken. Natural resource and disaster relief managers often will sacrifice accuracy for affordable, near real-time georeferenced assessment of the surveyed area.

This thesis presents a low-cost, end-to-end *system* for rapid single image geo-registration of airborne imagery collected from a small autonomous unmanned aerial vehicle. Custom electronic hardware is developed to facilitate easy user interaction with the UAV as well as

INS/Camera synchronization to perform direct georeferencing. A method of field calibration for the system is devised to provide fast, repeatable results. Mapping software called “PolarisView” was developed to register direct georeferenced images into Google Earth[®] post-flight in a rapid, near-real time manner.

A test flight over pre-surveyed targets is conducted to assess the initial accuracies of the direct georeferenced solution. By comparing the coordinates of the targets that lie within the overlaid Google Earth[®] image to that of their actual location, a measure of residuals was established. A 34 picture subset was selected for spatial comparison; a total of 62 instances of the control points were captured. It was determined that 4.9% of the control points were identified within a 25 meter radius of their actual location, 36.5% within 50 meters, 27.6% within 75 meters, 21.3% within 100 meters, and 9.8% within 150 meters. Therefore, a 67.62 meter RMS error exists in the direct georeferenced image solution across all measurements.

CHAPTER 1 INTRODUCTION

In many natural resource and civilian applications, frequent georeferenced high-resolution imagery is useful in answering numerous questions. Traditionally, satellites and specially-suited manned aircraft provide these services. However, for many reasons these technologies fall short of fulfilling the flexible, quick-response needs of natural resource management and disaster relief personnel. Therefore, a supplemental aerial mapping tool is necessary. Unmanned systems have proven themselves to be capable of achieving similar objectives as their manned predecessor and show much potential in filling the void in existing aerial mapping technologies. A small, inexpensive, quick-to-fly Unmanned Aerial Vehicle (UAV) could be the solution. Most small UAVs are used for surveillance and reconnaissance only and are not designed specifically for high resolution mapping applications. Researchers at the University of Florida are one step closer to being able to produce frequent, high resolution geo-registered still imagery from a small UAV.

Motivation

With the onset of personal computers and the internet, digital mapping technology is used on a regular basis. Maps and georeferenced information is accessible to a variety of people who need to make quick, informed decisions on a variety of issues; from emergency relief efforts to long term ecosystem management. Many of these maps are out of date and of low detail due to cost restraints within civilian funding agencies. Small Unmanned Aerial Systems (UAS) have been developed from high dollar military budgets for the last twenty years; consequently, this spending has provided the means of affordable technology that will be beneficial to an array of civilian agencies. First and foremost, UAVs can be used in certain applications to remove the element of risk from the human pilot in treacherous environments.

Traditional low altitude natural resource assessment is very costly and dangerous, but necessary in many situations where ground-based sampling is troublesome. “Using aerial photography can reduce costs by as much as 35% for the mapping, inventorying, and planning involved in the management of forest and rangelands” [1]. Natural resource managers and biologists are among many that look to benefit from civilian UAS technology. Biologists put their life on the line frequently to take aerial surveys that UAV technology could easily replace. In fact, small aircraft crashes are the leading cause of work-related death for wildlife biologists. “From 1937 to 2000, 66 percent of fatal accidents were contributed to small aircraft incidentals” [2]. Just recently (March 2008), a small Cessna crashed killing the pilot and three biologists conducting a wading bird survey in the Everglades [3]. Just two months later, a similar wading bird survey was performed by a UF UAV.

The University of Florida (UF) has been working for six years on a simple, inexpensive, hand-launchable UAV for wildlife and natural resource monitoring. This format UAV allows for easy storage, quick accessibility, and relatively safe operation for civilian use. Further, recent advances in digital imaging allow UAV platforms of this size to produce comparable quality images to that of low altitude man-collected imagery.

In 1999, the College of Natural Resources and Environment at the University of Florida initiated the UF Wildlife UAV program by conducting a feasibility study using a UAV to survey wildlife in a variety of habitats [4]. Several make-do and commercial off-the-shelf (COTS) platforms were tested and evaluated for their aerial imaging capabilities. These aircraft used progressive scan digital video cameras which produced decent imagery, but not of high resolution or georeferenced. Also, both aircraft used an unreliable nitromethane-gas engine that

ended up being the cause of failure and the surrender of both platforms. A better UAV platform was essential.

The Micro Air Vehicle Laboratory, part of the College of Mechanical and Aerospace Engineering, became collaborators of the Wildlife UAV program in 2002 and produced a much improved, specially designed electric-powered composite aircraft called the “Tadpole”. This platform was outfitted with better avionics and imaging capabilities [5]. However, improved sensor integration was necessary to acquire georeferenced imagery.

The Geomatics program at the University of Florida became involved in the program in 2005 and began working with image post-processing and georeferencing. The first application of the captured imagery from the UAV was to count populations of birds by an automatic detection algorithm [6]. Later, a study was performed over the National Bison Range to assess video georeferencing capabilities of the UAV. It was determined that in order to successfully georeference video frames, the platform needed: a better calibration procedure, a more accurate GPS/INS system and a better method for synchronizing UAV attitude and image exposure [7].

The Polaris UAV Overview

Since early 2007, the UF Wildlife UAV program has been focusing on many of the issues past literature expressed as “challenges” with a UAV platform of this size. The latest UF iteration, the Polaris UAV, addressed previous shortcomings by adding the elements of aquatic recovery, easy user control and directly georeferenced imagery. A parallel effort on a levee monitoring project for the Army Corps of Engineers inspired the development of the Polaris UAV. The 2004 version of the University of Florida airframe served as a base design for the Polaris since it had proven itself in tough operating environments [5].

The Polaris UAV was designed with a larger wing area in order to accommodate heavier camera payloads and a slower cruise speed. The Polaris uses simple full-function conventional

control; throttle, aileron, elevator and rudder. The Polaris UAV is an autonomous imaging system, meaning the aircraft is capable of tracking attitude, altitude, airspeed, and course without relying on human input for control. While under autonomous operation, the aircraft can perform synchronized digital imaging.

Power management circuitry was devised to eliminate the need for multiple batteries. All subsystems are now interfaced using customized circuit boards with reprogrammable microcontrollers; this allows for payload synchronization and control as well as mission specific changes and further development. The airframe and electrical components were made water-resistant for UAV water recovery.

A condensed version of the UAV ground station was conceived with dual touch screen monitors to be able to view all UAV controls and video output. A Windows Visual C++[®] user interface was designed to aid the user in inertial sensor calibration, payload camera interfacing, and exterior lighting control. Further, this software allows the user to control the synchronized automated picture capture function of the Polaris.

Output from the UAV includes synchronized digital images and aircraft state variables on two independent portable SD[®] memory cards. The dual memory card method reduces down time between UAV flights; the user has to simply replace both SD[®] cards and main battery to initiate another flight. The UAS was dubbed “Polaris” (as in the Polaris star) because of its bright white forward pointing LED.

Georeferencing and Rapid Mapping

In many instances, quick, moderately-accuracy single image mapping outweighs the long turnaround time of high spatial accuracy mosaics; assessment of levee structural conditions is one example. In order to achieve comparable resolution of expensive high altitude aircraft, small UAVs must compensate by flying closer to the ground, therefore reducing their field-of-capture.

Time and labor involved collecting ground control points necessary to improve the accuracies of small footprint photos through indirect georeferencing contradict the usefulness of the quick-to-fly abilities of the small UAV. Further, most areas in which UAVs are useful are nearly inaccessible to place ground control points. Therefore, the Polaris UAV uses a newer concept of direct georeferencing to determine photographic area extents.

Unlike many small UAS that only use wirelessly transmitted video for imaging, the Polaris uses a modified COTS digital frame camera to collect high-resolution images during autonomous operation. The commercial point-and-shoot cameras are not metric imaging devices and require additional calibration steps to be useful in mapping applications. A calibration procedure is developed through a well documented Matlab[®] camera calibration toolbox [8].

The COTS software does have the ability to handle direct georeferencing input, but often requires a great deal of human interaction to produce usable results. Further, commercially available software limits flexibilities in adapting to advancements in the platform. Consequently, a Matlab[®]-based graphical user interface called PolarisView was developed to handle the post-processing and mapping of the Polaris output data in an automated, rapid fashion. The formatted, georeferenced images are importable into a geographic information system (GIS) such as Google Earth[®] for further spatial analysis.

CHAPTER 2 LITERATURE REVIEW

UAV technology has proven itself very useful in the Iraq battlefield as well as in other hostile environments. The same capabilities of unmanned systems used in warfare will contribute to a multitude of civilian applications in the coming years. Each size class of UAV has its own niche in the spectrum of mission requirements. For many reasons, the small electric UAV continues to be the favorite amongst wildlife biologists and ecologists. The advancement of imaging systems and power generation technology will pave the way for the future generations of small unmanned aerial mapping systems.

Small Unmanned Aerial Vehicles

The majority of the research and development of small unmanned aerial vehicles has been in the military context. However, their successes have spurred many new applications in other civilian interests. Configurations and sizes of UAV's vary greatly with application, but the focus here is on small, fixed-wing unmanned aerial vehicles.

A small UAV is defined by the army as having less than a 4 meter wingspan and weighing less than 55 pounds [9]. The term Unmanned Aerial Vehicle has been recently renamed by the Department of Defense and the Federal Aviation Administration to the Unmanned Aircraft System (UAS), but is used interchangeably throughout this paper [10]. The inception of small UAV technology began with the creation of the AeroVironment® Pointer in the late 1980's [11]. UAS technology remained somewhat undeveloped until 1996, when Defense Advanced Research Projects Agency (DARPA) launched its Micro Air Vehicle (MAV) program. In 2001, DARPA began focusing on the mission capability aspect of MAV's and funded many projects that produced tiny aircraft such as the AeroVironment® Black Widow to be used in covert military operations [12]. Academic ventures such as the International Micro Air Vehicle

Competition sought to unveil new methods and technologies for creating these undetectable micro aircraft. The University of Florida has been extremely successful in this competition, winning seven of the eight years they competed. Compliant, wind gust-alleviating composite aircraft developed at UF was the contributing factor to numerous successes [13],[14], [15]. Similar technology has been implemented on deployed small UAV platforms used by the military [16].

Research efforts eventually shifted back from MAVs to small UAVs due to the very limited payload capabilities and endurance. The primary use for small UAS platforms has been for surveillance and reconnaissance, however payload capabilities of this size class UAV are attracting use in other remote sensing applications. Many academic institutions are assessing a variety of research topics that will benefit many civilian prospects [17],[18],[19]. Small UAV's have been used for many different precision agricultural applications such as vegetation monitoring and crop yield estimation [20], [21], [22], [23]. UAS have even been used for more exotic exploratory endeavors such as volcanic gas sampling, forest fire monitoring and hurricane research, where aircrew of manned missions were at the greatest risk [24],[19], [25].

Aerial Imaging and Georeferencing

Many different kinds of imaging payloads exist for small aerial vehicles. Common imaging sensors used in modern small UAV's include visible spectrum, infra-red and thermal infrared imagers. All have different optics and measurable wavelengths, but still adhere to the same photogrammetric principles needed for georeferencing.

Two forms of georeferencing exist for computing desired spatial relativities. Indirect georeferencing uses ground control points to back-calculate the external orientation parameters of the imaging sensor [21]. Direct georeferencing estimates ground coordinates based on attitude and positional measurements made on the aircraft [26].

Several methods of indirect georeferencing exist and are used widely among UAS. One such process called “image-to-image” georeferencing uses common tie points between two images to register one image to the other [27],[7]. “Image-to-Map” georeferencing uses identifiable ground control points in each image to perform a transformation from pixel row/column information to aircraft orientation needed for locating other ground locations in the image [28]. Another form of indirect georeferencing is called aerial triangulation. This procedure uses identical object points in two separate photographs to determine height and position estimates [29].

Directly georeferenced images require synchronizing the timings of sampled position and orientation estimates of the aircraft with the camera’s exposure [18]. Rigid body transformations of the imaging plane element projections and intrinsic camera parameters allow ground coordinates to be determined [26]. Attitude and position estimates used for direct georeferencing in small UAVs are generally provided by their navigation instrumentation. Integrated low-cost global positioning system (GPS) and microelectromechanical systems (MEMS) based strap-down inertial measurement units (IMU) are popular guidance systems amongst small UAVs. This technology is used for the benefit of reduced size and weight; however forfeits position and attitude accuracies. Boresight, the rotation of the imaging sensor versus the IMU and lever arm offsets, distance between imaging sensor and IMU, must be taken into account in the georeferencing solution [30].

Small UAV’s are lightweight, low altitude aircraft and are therefore susceptible to wind turbulence and high dynamic situations rendering attitude estimation and synchronization non-trivial. Atmospheric conditions are more suitable for vertical imaging from high altitude UAVs, however, cloud cover at these altitudes can cause obstructed landscape. Few small UAS’ in

literature use direct georeferencing, however, much faster mapping results can be achieved when low-accuracy is acceptable [29]. High accuracy rapid direct georeferencing systems do exist on sizable manned aircraft but have not been refined for smaller, less-accurate UAV systems [31].

Both forms of georeferencing require the determination of interior and exterior camera parameters. Interior constituents consist of camera parameters such as effective focal length, scale factor, principle point offset and lens distortion [32]. Exterior parameters are a function of sequential rigid body rotations describing the relationship between the image plane and the world coordinate frame. Many methods for determining interior and exterior camera parameters exist, but all have a similar underlying process; satisfy the collinearity condition based on known spatial locations. “The collinearity condition guarantees that at the exposure station, an object point in the mapping frame and its photo image in the image plane all lie along the same line in three-dimensional space” [7]. The selected process for determining the camera sensor model used for the Polaris platform is very comprehensive and includes both radial and tangential lens distortion components that can be used to correct image distortion and projective geometry extents [33].

Digital Mapping

Projective geometry is used to predict image coverage extents and is a function of tilt about all axes of the aerial platform [34]. However, acquiring the ground coordinates of the captured area is only a start in the mapping process. A geometric distortion exists in any non-vertical photograph and must be removed before the image can be registered into a reference datum [26].

Geo-registration is the process of flattening tilted images until their normal vector is parallel to the mapping system’s normal vector in a georeferenced location [27]. Differential orthorectification accounts for distortions in the photo caused by height differences of elements that span a photograph [34]. This case is not considered for Polaris image mapping, but is a

focus for future research. Aerial imaging platforms using film cameras require mechanical and optical equipment to remove tilt distortions in the photographs, which is a very time consuming manual process [34]. With the inception of digital imaging, these processes are no longer necessary. Digital rectification requires the use of digital image processing to resample the raster data to create an undistorted digital image [35]. The resampling process alters the row/column makeup of the digital image based on projective geometry constraints to allow the output image elements to cover equal units of area; as if the image was taken vertical to the ground. The increase in computing performance over the last ten years allows for high pixel-count (high resolution) digital images to be rectified quickly. The assembled map can then be used for various ecological photo interpretations such as grid sampling, where information about a viewed area can be extrapolated to predict tendencies in larger areas [27].

CHAPTER 3 POLARIS UAV AIRFRAME

The University of Florida's Micro Air Vehicle (MAV) Laboratory has been developing small and micro unmanned air vehicles for almost twelve years now. The laboratory's expertise in composite materials and manufacturing has allowed for the development of some of the smallest and lightweight flying planes in the world. The design and construction methodologies of the MAV laboratory has always been iterative and geared toward rapid, inexpensive, mission capable composite aircraft that are easy to fabricate and assemble. Past UF UAVs were driving factors in the Polaris design. The following gives a brief overview of the design and construction of the Polaris airframe as well as the electronic equipment associated with the current technology.

Construction

The Polaris UAV demanded more unique marine operating environments than its predecessors, so several different construction materials and techniques were employed. Polaris' design was easy to construct for someone with intermediate level of composite material experience. The UAVs' conventional layout and modular design allows for fast field assembly and easy replacement of damaged parts.

The fuselage design of the Polaris UAV remained identical to the previous UF design (Figure 3-1) [5]. The Polaris UAV was designed using lightweight materials and methods to keep overall airframe weight to a minimum. The fuselage was constructed out of 189.9 grams/sq meter woven Kevlar® fabric and a high strength epoxy-based resin rendering an exemplary strength to weight ratio and very abrasion resistant. The motor mount portion of the fuselage was reinforced with a 193.3 grams/sq meter carbon fiber cloth for rigidity. The fuselage was dunk-tested to ensure it was free of water leaks; any voids were patched with a fast drying two

part epoxy. A fiberglass hatch was made from a rubber-plugged female mold that was machined from high density foam tooling-board.

The wing and tail sections of the Polaris UAV were made of a fiberglass wrapped low-density Styrofoam and epoxy-doped balsa stock. Wing and tail section designs were sent away to Flyingfoam.com to be hotwire cut out of large blocks of 16.0 kilogram per cubic meter EPS foam. This foam was selected for its sparse closed-form porous surface allowing adequate infusion of epoxy from the wrapped fiberglass skin; this keeps the fiberglass cloth from delaminating from the foam.

Table 3-1 shows all wing and stabilizer design parameters. Figure 3-2 shows the planform of the wing and stabilizer sections. The wing sections had three holes and span-wise rectangular grooves made during the hotwire cutting process. Two of the holes were cut mid-span into the wing and were reinforced with cardboard tubing to accommodate the carbon fiber wing joining spars. The largest hole for the load bearing spar was 21 millimeters in diameter while the torsion tube hole was 14 millimeters. The third hole was cut full span length at center chord to accommodate the electrical wiring throughout the wings. Span-wise grooves facilitated square 4.8 millimeter balsa stock to aid in bending rigidity. Epoxy-doped spruce hardwood was placed in critical areas in the wing and stabilizer sections for fastening and mounting. Control surfaces were cut from the EPS blanks and hinged with a rectangular piece aramid fabric.

All wing and stabilizer sections were wrapped with 115.3 grams/sq meter s-glass (structural fiberglass) fabric then wet with a slow cure, high strength epoxy resin and tensioned with low-density acetate release film for a nice surface finish (Figure 3-3). Wet sections were then placed in their respective female portion (shuck) of the original EPS block to keep shape while under external weighting (Figure 3-4). After a full twenty-four hour cure, hardened

sections were removed from their shucks and touched-up with a lightweight, foam-safe filler to fill any pinhole water leaks.

Assembly

All fuselage, hatch, wing and stabilizer sections were sanded and painted their respective coloring; blue and orange of course. An epoxy-doped piece of 1.5 mm spruce hardwood shaped as the cross section of the fuselage was glued into place to serve as a primary bulkhead for initial strengthening. A 19 millimeter diameter, 1 meter long carbon fiber tube was fitted through the back of the fuselage and mated with an accommodating hole in the center of the bulkhead inside the fuselage. The carbon tube was glued into place at all contact points using Hysol[®] adhesive. Holes were cut out of the fuselage for the forward pointing white LED (light emitting diode), female camera lens insert, speed control, video transmitter, forward looking camera, pitot tube and on/off switches. Stainless steel 3 mm screw/nut pairs were installed on the four corners of the hatch opening to serve as o-ring posts to hold down the hatch during flight. A receiving “saddle” for flush wing/fuse interaction was made out of fiberglass. Two 9.5 mm carbon fiber dowels were installed approximately 28 millimeters below the saddle to serve as rubber band wing fastener posts. A 6.4 mm carbon tube along with plastic tubing was installed in the nose of the fuse to serve as a Pitot tube. Plastic tubing was connected to a y- junction plastic housing with water catch to keep water away from the dynamic pressure sensor of the autopilot in the instance of a water landing.

A 304 mm section of the carbon fiber tube was cut off the back of the tail boom to be used for stabilizer mounting. The motor was installed onto the fuselage with stainless steel hardware and the motor wiring was sealed with a rubber grommet and ran into the fuselage. Marine grade weather stripping was installed around the wing saddle and main hatch lip to form a water resistant seal when hatch and wings are installed. A carbon fiber sheet was laid up and cut into

an ovular shape to fit snugly in the upper third of the fuselage; this formed a hatch that was siliconed into place to keep water out, but could be removed if necessary (Figure 3-5). The cable for the wings and a programming header was installed here in this “saddle hatch”. Two on/off switches were rubber booted and installed into the back of the fuselage above the tail boom for easy access.

Wing and stabilizer control surface areas were scored and cut appropriately to allow adequate deflections. Titanium control clevises with plastic stop horns were installed on all control surfaces. Servos were mounted in all EPS wing and stabilizer cores using a plastic servo mounting tray that facilitated easy servo replacement. Servo hatches were devised out of flat pieces of fiberglass that had rectangular holes made in them so that a rubber servo arm boot could be installed to isolate water from the servo chamber.

Four 12.7 mm neodymium magnets were installed into the root of each wing to serve as wing joiners. Red and Green LED's with complete wiring were installed at the tips of the wings and a white LED was installed at the top of the vertical stabilizer. All LEDs were covered with a plastic globe for waterproofing. Guides were cut in the trailing edge of the wing near the root to accommodate the rubber bands used for wing attachment to the fuselage.

Holes were drilled into hardwood sections of the horizontal stabilizer so it could mate with aluminum tail boom mounting hardware (Figure 3-6). Two vertically mounted 5 mm carbon tubes were ran through the horizontal stabilizer and were used to support the vertical stabilizer to the separated tail boom section. An access hatch was cut out of the vertical stabilizer for radio modem installation and connectivity.

A carbon tube fitting the inside diameter of the tail boom was glued into place to serve as a coupling between tail boom and tail section. A 6.4 millimeter stainless steel screw/nut set was

used to fasten the tail to the tail boom. A cap was made for the open end of the tail section for waterproofing. Figure 3-7 shows a completed Polaris UAV airframe.

Initial flight testing was conducted with just the airframe and COTS radio-controlled electronic hardware. The plane was outfitted with early generations of the customized electronic hardware to collect and wirelessly transmit power draw and temperature readings of critical flight components to ensure reliability for real missions. The initial flight platform proved it could fly for 50 minutes on a single 10000 mAh, 18.4V Lithium-Polymer battery. This was the battery chosen to be used in actual missions. However, a smaller capacity, lighter battery could be used to offset the weight of heavier future payloads. Mission flight times were restricted to 40 minutes for safety. It was determined that an airspeed of 14 meters/second was as safe flying speed for the aircraft and provided a slow enough ground speed for sharp images. A critical airspeed of 10 meters/second would cause the aircraft to stall.

The finalized aircraft conducted missions in the actual habitats it was designed for. Mission take-off scenarios including land, motor boat and airboat were all very successful (Figure 3-8). Landings were accomplished on land, in open water, and within marshy, cattail lined wetlands. Day and low-light missions were successfully tested as well (Figure 3-9). Protocol for mapping missions entailed manually flying the plane from hand-launch up to a safe altitude (approx. 100 meters) then engaging autopilot control for the majority of the flight. During this time, flight coverage area, altitude or payload settings could be altered using the ground station interface. Also, the UAV could be toggled in and out of synchronized image capture mode. After the survey was completed, the Polaris was landed using manual control.

Table 3-1. Wing and stabilizer design parameters

Section	Airfoil	Span	Root Chord	Tip Chord	Sweep	Washout
Wing	NACA2313	2.4384 m	0.3048 m	0.2032 m	1.19 deg	2.5 deg
Horizontal Stab	NACA0012	0.6913 m	0.2095 m	0.1168 m	3.83 deg	0 deg
Vertical Stab	NACA0012	0.36957 m	0.2286 m	0.1295 m	3.83 deg	0 deg



Figure 3-1. Unpainted Kevlar[®] Fuselage used for the Polaris UAV

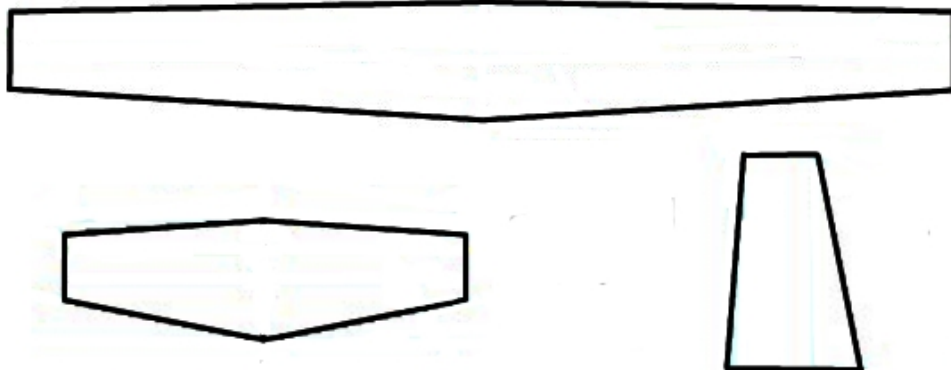


Figure 3-2. Polaris' wing, horizontal and vertical stabilizer plan forms

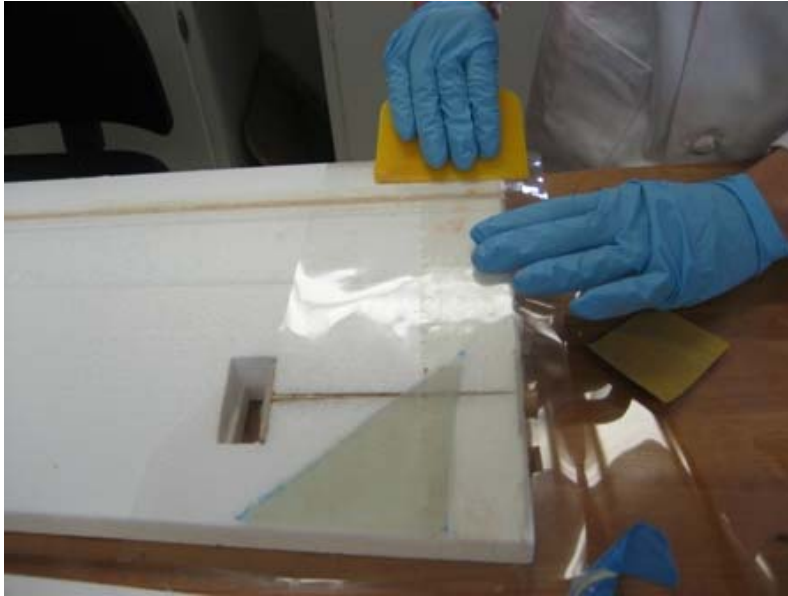


Figure 3-3. Tensioning acetate film over fiberglass skinning creating a smooth external surface.



Figure 3-4. Process for compressing fiberglass curing epoxy to EPS foam wing cores



Figure 3-5. Saddle hatch for programming access of PDIB processor and wing connectivity



Figure 3-6. Horizontal stabilizer tail boom mounting hardware

A

B



Figure 3-7. Completed Polaris UAV airframe A) Bird's eye view B) side view



Figure 3-8. Airboat launch and recovery setup. The mission was conducted in an Everglades marshy environment.



Figure 3-9. Polaris day and low-light flying configuration

CHAPTER 4 POLARIS UAV ELECTRONICS

The end goal of the development of the Polaris UAV was to keep everything as inexpensive, reliable, simple, and “hand-launchable” as possible in order to conduct aerial surveys. Since the Polaris is of the same size as many model aircraft, quality COTS hobby components were used in order to reduce time-to-flight as well as cost. Some of these components were slightly modified in order to meet our goals, such as waterproofing. However, when it came to power management, synchronous imaging, data collection and systems integration, there were no solutions available in our size, weight, and cost budget. Therefore, custom electronics were developed for special use on the Polaris UAV. All custom printed circuit boards are two layer boards and were designed using Altium Design Explorer®. All printed circuit boards were exported to Advanced Circuits for manufacturing and populated at laboratory facilities at UF. Every form of electronic circuit board was encapsulated with MG Chemicals® brand encapsulating compound to ensure water-resistant, vibration proof operation. Certain components were covered with thermally conductive encapsulating compound depending on heat dissipation requirements.

Motor Selection and Controller

Previous versions of the University of Florida UAV used a nitromethane internal combustion engine that proved to be very messy, noisy, and unreliable. The prequel to the Polaris had an electric motor that performed very well [5]. An E-Flite 46 860 KV, brushless outrunner motor was selected for the Polaris because of its increased torque and improved cooling. Also, it is inherently waterproof in operation; a great advantage over brushed motor technologies. The basic concept of brushless motor technology involves using variable induction rather than electro-mechanical brushes for torque generation. There is no electrical contact to

short in case of water recovery. (The motor bearings and iron cores were sprayed thoroughly with silicon-based lubrication after each water landing.)

A Jeti® 70 Amp brushless speed control was selected to control the UAV's electric motor. This speed control surpasses the maximum amperage draw for the motor considerably as to ensure reliability. The entire speed control was covered in a thermally conductive epoxy and a 50.80 mm by 13.46 mm by 4.83 mm finned heatsink was added to ensure reliable performance. The motor/speed control combination produces approximately 1025 watts of power with a 10x8 three-bladed propeller, which produces adequate hand-launchable takeoff thrust.

Actuators

The Polaris UAV uses servomechanisms (servos) for actuation of control surfaces. Wing and stabilizer sections were designed for the servo to be installed within them; therefore a low-profile, thin servo was required. The JR® model DS168 digital thin-wing metal-gear servo was selected for the Polaris UAV. The DS168 is 6-volt tolerant and has substantial torque for its size. The servo exhibits .374 Newton-meter of torque at 6 volts and travels 60 degrees in 0.14 seconds.

Autopilot

The UF MAV Laboratory has been working with the Procerus Technologies® autopilots through several of their iterations. The latest version of the Kestrel autopilot has proven itself very reliable and was therefore selected for use on the Polaris UAV. Offering a rich feature set, the Kestrel v2.23 makes integration and setup a seamless process [36].

The Kestrel v2.23 weighs only 16.65 grams and occupies less than 21.11 cubic centimeters (Figure 4-1). The autopilot uses a temperature compensated MEMs-based three-axis gyroscope/accelerometer as the inertial measurement unit (IMU). The autopilot has a three-axis magnetometer and GPS for navigation. It has been reported in literature that this specific

INS/GPS navigation suite is capable of accuracies shown in Table 4-1 in near level conditions with post-processing [30].

The Kestrel v2.23 has 3 servo and 1 speed control output. A barometric pressure port is used for altitude estimation while a differential pressure port is used for airspeed estimation. The Kestrel v2.23 also has an open configurable serial port for external payload interfacing. Customized circuitry developed for the Polaris UAV is interfaced through this port. A Maxstream® 1 Watt 900 MHz radio modem is used to communicate with the ground station and is mounted in the vertical stabilizer to avoid electromagnetic interference (EMI) with other sensitive electronics (Figure 4-2). The autopilot was encased in a carbon fiber box for protection and waterproofing (Figure 4-3). External connectors provide signal and power routing.

The autopilot uses a combination of feedback and feed-forward control to stabilize and navigate the aircraft. Proportional-Integral-Derivative (PID) feedback controllers are used to regulate aircraft states and a feed-forward effort is applied in certain scenarios such as turns. All control loops have user defined saturation limiting to ensure aircraft stability and undesired aerodynamic loading. A real-time PID data logger in the user-interface was used for tuning the PID controllers while flying the UAV for the first time. Figures 4-4 through 4-6 show all control loop structures used in the Kestrel v2.23. During straight flight paths, the autopilot does an exceptional job holding the aircraft to its calibrated level condition. Only during situations of external excitation, such as turbulent wind, do the controllers have a difficult time commanding the UAV to remain level.

Global Positioning System Receiver

The Global Positioning System is the critical element of the INS/GPS integration that allows small UAVs to navigate with reasonable accuracy. For the size class of the Polaris, many COTS receivers are available. However, only certain units are compatible with the autopilot.

The GPS receiver used on the Polaris is a Furuno[®] GH81 model (Figure 4-7). This model is a low-power, 3.3 volt, 16 channel GPS with 15 meter horizontal accuracy (2drms) and 22 meter vertical accuracy (2drms). The GPS receiver is actually mounted on a printed circuit board and ground plane provided from Procerus[®]. The receiver is mounted on the right wing 40 centimeters from center. The GPS receiver is covered with a non-conductive plastic housing for splash resistance.

Subsystem Control Hardware

Synchronization amongst the payload imaging sensor and the autopilot are necessary to accomplish direct georeferencing. Further, the abilities to adjust functions of the payload while in flight were necessary. To integrate the payload sensor and other Polaris subsystems, customized electronics were required.

Since the decision was made to retain the fuselage from the Tadpole design, special considerations for physical circuitry layout had to be considered in order to remain within the physical constraints of the fuselage. The subsystem interface hardware, named the power-distribution-and-integration-board (PDIB), was designed to have a multipart role in the Polaris. The PDIB was fabricated on rigid, 1.6 millimeter thick FR-4 substrate and served both as a functional printed circuit board and as a secondary bulkhead for further fuselage reinforcement. A hole in the center of the PDIB allowed it to mate with the internal portion of tail boom and pass electrical cabling to the tail.

The outer most boundary of the printed circuit board was designed using AutoCAD[®], a computer-aided design (CAD) tool, to match that of the cross-section (bulkhead) of the Kevlar[®] fuselage. The CAD outline was imported as a keep-out-layer into the circuit design and board-level layout suite called Design Explorer[®], created by Altium[®]. The PDIB operates as an embedded system with an 8 Mhz Atmel[®] Atmega 128 8-bit RISC microcontroller as the central

controlling unit (Figure 4-8). Since the PDIB board was secured into place, the In-System-Program feature of the Atmega allowed for the microcontroller to be re-programmed without having to remove any other peripherals. A programming port was installed via a RJ-11 jack located near the top of the fuselage in the saddle hatch for easy accessibility. The microcontroller unit (MCU) has many features that can be seen in [37]. The Atmega 128 MCU was particularly selected because of the dual programmable universal synchronous/asynchronous receive/transmit serial ports. These serial lines were used to interface the payload, the autopilot and the SD[®] card writer/reader, which made camera/INS/GPS synchronization possible.

The USART1 receive port of the MCU accepted signals from the autopilot's SERIAL-A passthrough port via a 38400 baud, 8 bit word length, 2 stop bit serial structure. The USART1 transmit port was used to generate 57600 baud American Standard Code for Information Interchange (ASCII) messages to the SD[®] card writer. USART0 receive port listens to 115200 baud serial messages sent from the autopilot to the wireless modem containing aircraft state data used for camera synchronization. Lastly, the USART0 transmit line (57600 baud) is used to talk to the Atmel[®] Atmega8 MCU on the custom camera interface board or with any other payload that uses serial communication.

The MCU input/output (I/O) was also used to control the duty cycle (on-time versus off-time) of the Phillips[®] Luxeon 1 Watt low-light operation LEDs via power transistors. Digital I/O toggles a video multiplexer that controls signal routing from the payload camera and forward-looking CCD camera to the wireless video transmitter. The MCU's 10 bit Analog-to-Digital (ADC) ports were used during UAV testing for data collection of various external analog sensors. During normal autonomous imaging operation, the ADC samples a variety of voltages

in the design to check for power management failures. Ten additional digital I/O's were pulled out for future expandability.

Data Storage

Usually more than 400 high resolution digital images are taken every Polaris flight. These digital images are 12.1 mega pixels and can take up as much as 6.2 megabytes in file size, which equates to approximately 3 gigabytes of imaging data. This large amount of data could take as much as twenty minutes to transfer to the ground station computer before another flight could commence. Therefore, inexpensive portable memory was chosen over a USB 2.0 transfer method. Wiring was run from the payload box to an externally mounted SD[®] memory card holder so that the camera's built-in memory management features could be used. After each flight the memory card was removed and replaced with a formatted card of the same size.

UAV state data storage was accomplished in a similar fashion. A lightweight memory card management module with a DosonChip[®] was selected to write serial ASCII data from the Atmega 128 (Figure 4-9). The DosonChip[®] allows for easy memory card management having file structures similar to MS-DOS[®]. The card has poor throughput, but was adequate to handle the 200 bytes/sec needed. Every time a picture is taken, a single file called, PIC_DATA.txt, is appended with space delimited UAV state data and terminated with a carriage return. A typical text file size for a 400 picture mission is roughly 70 kilobytes, so only a small SD card (250 MB) was used. Other articles of data, such as camera calibration and positional parameters, share space on this card for digital mapping purposes.

Cameras

The Polaris UAV has two cameras on-board for different purposes. The first camera is a CCD chip camera used as a "situational awareness" camera giving the operator a first-hand look through the front of the UAV. The second camera was the payload camera whose type was

dependent on mission application. All testing with the UAS has been with a digital camera payload for direct georeferencing testing, however, other sensors, such as a thermal-infrared imager is awaiting installation.

The CCD chip camera circuitry was sealed with encapsulating epoxy and installed in the nose of the Polaris (Figure 4-10). The 5 volt, KX-141, 13 gram, 640 x 480 resolution, color CCD video imager was selected as the forward looking camera (Figure 4-10). The NTSC output of this camera was multiplexed with the payload's camera NTSC output for toggling of live video via a 1 Watt wireless 2.4 GHz transmitter. Live forward looking video also provided visual aid in control loop tuning and manual landing exercises. The transmitter and custom video control circuitry generated large amounts of heat, so they were encapsulated in thermally conductive epoxy and mounted on a common external heatsink for heat dissipation (Figure 4-11).

The digital imaging payload used in the UAS was a COTS Canon A650 12.1 mega-pixel point and shoot camera which provided 25 mm pixel ground coverage at 100 meter altitude. The camera was stripped of all non-imaging elements such as the flash, battery holder and any other unnecessary casing, shaving off about 35% of its total weight (Figure 4-12). A lightweight, carbon fiber housing with 52 millimeter lens cover was made to protect and waterproof the camera's internal components. The housing was lined with low-density foam to isolate the sensor from vibrations.

Originally, the use of an IEEE1394 protocol for controllability of the A650 was tested, however, it was not possible to control the manual focus functionality of the camera. A manual focus setting at infinity reduces static shutter lag compared to the dynamic behavior of the

camera's built in auto-focus function. A PCB was designed with an Atmel® Atmega 8 MCU to control the Canon A650 digital camera hardware (Figure 4-13) [38].

The custom camera controller board received serial commands from the Atmega 128 on the PDIB to control all aspects of the camera, including going in between still picture and video mode. Digital I/O signals were run from the Atmega8 MCU to all input buttons of the Canon A650 hardware. Insulating Kapton® tape was used to secure the circuit board and wiring to prevent shorting. A digital oscilloscope was used to capture the waveforms needed to “trick” the camera into thinking a button was pressed. The waveforms were regenerated on the Atmega8 at desired times, acting like a very fast “digital finger”. A source-able line driver was used to trigger the camera to turn on and off. Power was provided to the camera and controller board from the power module described below.

Polaris Power Management

The previous version of the University of Florida UAV required three separate battery packs in order to operate all subsystems; this became troublesome between flights when the wings had to be removed in order to change these batteries. Also, no voltage level indication from two of the three battery supplies was available. Therefore, a power regulation design was implemented that allowed for only a single battery to be used. There are many issues that arise during efficient DC/DC power management, especially in large voltage differential situations as the case on the Polaris UAV. Multiple iterations were made to the power design and tested for airworthiness. A DC/DC step-down solution was developed that is flexible for future platforms and proved to be very reliable.

The primary concern for the power management design involved reducing as much as 21.2 volts, from a fully-charged battery, down to no greater than 6 V for UAV components. Heat

dissipation is usually a concern in this scenario. Sensitive digital circuitry was used in the aircraft, so voltage levels needed to be well conditioned.

The power management design was a hybrid of switching and linear voltage regulators. The design is cascaded and separated into two categories of electronics; noise-sensitive and non-sensitive. The front-end voltage regulation is done with a high-power switching regulator and is used to power non-sensitive devices such as LEDs, servos and camera payload (which has its own set of regulators). The remaining voltage regulation is done with linear regulators. All the current to power the system has to be sourced from the switching regulator which has a much better heat dissipation property to that of linear architecture. The video transmitter is the only device that uses a straight linear regulator from the input battery; however, it only has to step down to 12 volts instead of 6 volts.

The switching voltage regulator that was chosen to do the front-end power regulation was a National Semiconductor® LM2677 Series adjustable voltage regulator in the LPP (Leadless Plastic Package) package. This regulator can source up to five amps and can accept a wide input voltage range (between 8 to 40 volts). The output voltage is adjustable from 1.2 volts up to the input voltage. The internal switching frequency is between 225kHz – 280kHz depending on output voltage. A two resistor bias network exists to alter the adjustable output voltage. A 5.8 volt output from the regulator was selected in order to remain within operating limits of other electrical components. A special PCB layout was devised for this regulator so that the design could be inserted into other circuitry using 2.54 millimeter pitch male headers.

The small, output-adjustable, easy mounting voltage regulation board was called the “power module”. The power module operates between 85-88% efficiency depending on instantaneous current output (Figure 4-14). A ground plane on the bottom of the board and

aluminum rectangular shielding was used to help reduce EMI of neighboring circuits.

Approximately 9 Watts is available to the payload to keep the power module within a safe operating range.

A 5 volt and 3.3 volt linear regulator was used after the power module output for more sensitive electronics where stability and voltage ripple are more critical. Both microcontrollers and the GPS receiver were powered with these supplies.

Ground Control Station

The ground control station (GCS) serves as the critical link between the UAV and ground operators. Many modifications were made to the GCS over past years renditions for ease of use and reliability. The housing of the GCS is a watertight, wheeled Pelican[®] case with external peripheral interfaces (Figure 4-15). A Panasonic Toughbook[®] is the central piece of equipment in the GCS. This laptop computer runs the Virtual Cockpit, PolarisLink and PolarisView software packages. Both monitors provide a way to distribute the multiple software GUIs spaciouly so everything is accessible quickly.

The GCS has a Commboss provided by Procerus Technologies[®] with the matching 900 MHz radio modem for wireless communication and an external jack for connecting the manual pilot control box for take-offs and landings. The GCS uses half-wave monopole antennas for both video and telemetry reception and transmission. However, weatherproof N-type coaxial connectors are provided externally so that larger, more directional arrays can be connected for increased communication range. The Commboss interfaces the laptop computer via a standard serial cable. The GCS has a 2.4 GHz video signal receiver for displaying live video feeds from the Polaris. Video overlay of system critical information is viewable over this feed. The laptop has an analog video frame-grabber for recording live video streams. The GCS uses an AC/DC 140W converter to power electronics in instances where AC power is accessible. This is useful

for flight planning indoors. All critical flight electronics in the GCS have battery-back built in. A weatherproof USB port and DC cigarette lighter port are provided for east accessibility.

Table 4-1. Root-mean-square errors in the Kestrel v2.2 INS/GPS in near level conditions (<~4 degrees)

Roll (Deg)	Pitch (Deg)	Heading (Deg)	Northing (m)	Easting (m)	Altitude (m)
0.44	0.31	1.1	0.90	1.0	2.1

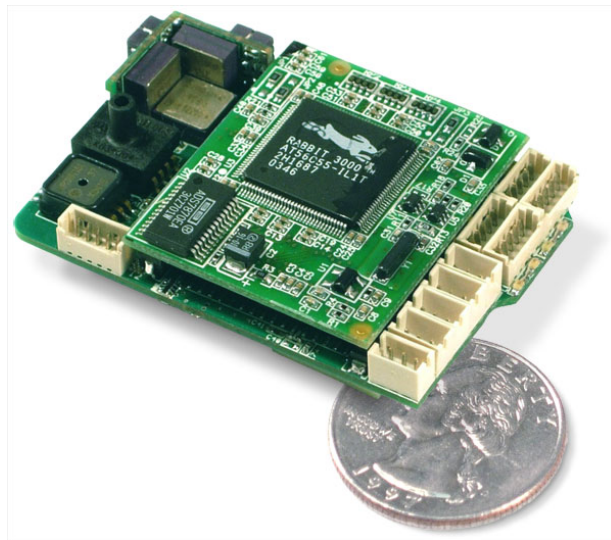


Figure 4-1. Procerus® Autopilot - Kestrel v2.2



Figure 4-2. One Watt Aerocom modem is mounted in tail to reduce EMI



Figure 4-3. Carbon fiber box for autopilot with waterproof interfacing electrical connectors

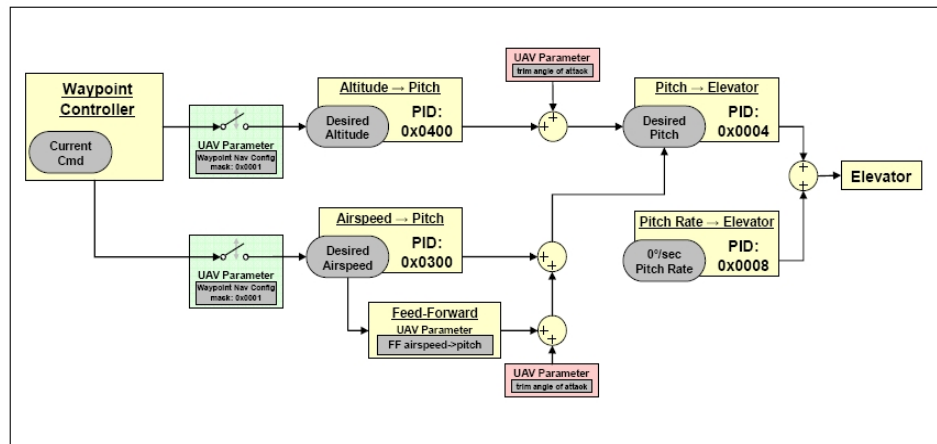


Figure 4-4. Elevator control loop

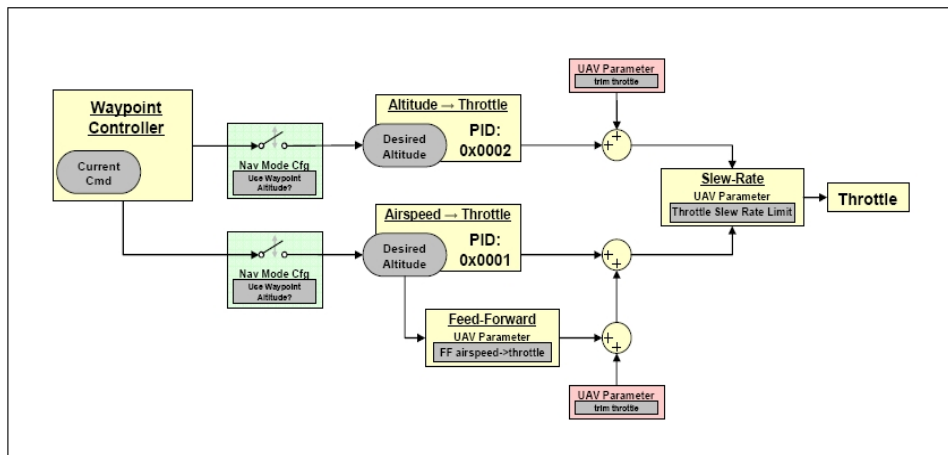


Figure 4-5. Throttle control loop

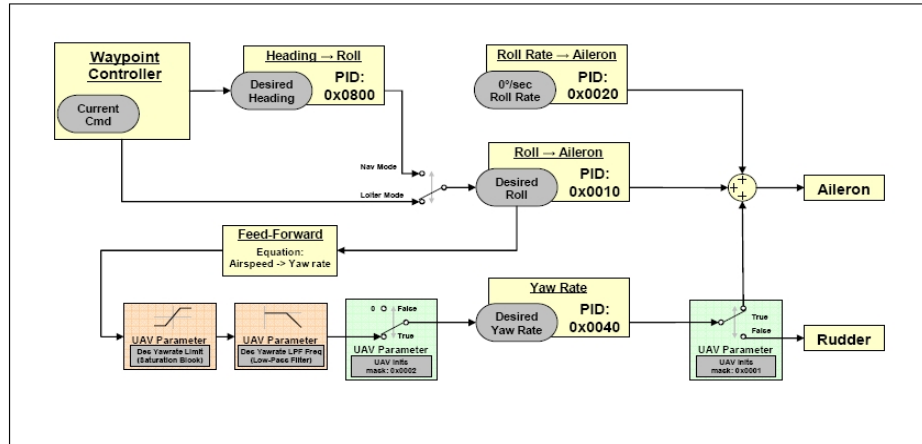


Figure 4-6. Aileron/Rudder control loop

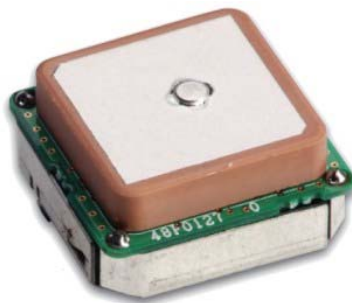


Figure 4-7. Furuno GH81 GPS receiver on Polaris UAV

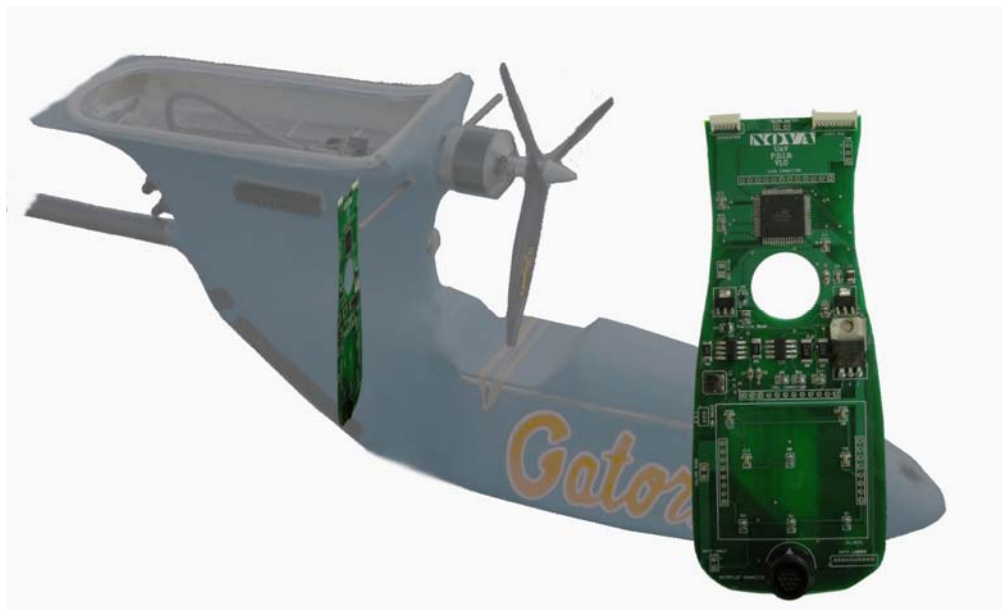


Figure 4-8. Custom designed “Power Distribution and Integration Board”. Figure shows placement of printed circuit board within the fuselage. Note: The Power Module is not installed in this figure.



Figure 4-9. DosonChip SD Memory Card hardware used to store synchronized UAV orientation and location data



Figure 4-10. KX-141 CCD camera and installation location



Figure 4-11. One watt video transmitter (no antenna) and video control circuitry. Thermally conductive epoxy was later used on the components for waterproofing. An externally mounted heatsink was used for heat dissipation.



Figure 4-15. Front and back of Ground Control Station (GCS)

CHAPTER 5 POLARIS UAV SOFTWARE

Previous UF UAV platforms performed well for imaging and flight data collection, but provided no means for sensor interfacing, synchronization or georeferencing. The Polaris UAV was designed with programmable microcontrollers that would allow for system upgrading and specific mission changes. Further, a Graphical User Interface (GUI) was developed for Windows[®] that gives the user complete control of UAS peripherals in real-time.

Firmware

Firmware is software compiled to run at the processor binary level from some higher level language. Both Atmel[®] microcontrollers were programmed with firmware generated from the CodeVision AVR[®] C Compiler. Each microcontroller is responsible for separate tasks, but share information amongst each other via a serial data link. A custom serial communications protocol was developed to pass data from the ground station software to the dual UAS MCU's.

The primary MCU, the Atmega 128, managed a wide variety of tasks to carry out autonomous mapping functionality. This MCU was programmed to: issue commands to the payload, extract high rate UAV state data, generate synchronized camera shutter capture, control onboard video selection, generate pulse width modulation (PWM) signals for LEDs and write out data to the portable SD[®] memory card (Figure 5-1).

The autopilot was configured to use the SERIAL A port as a pass-through port, enabling wireless serial messages generated from PolarisLink to “pass through” this bus to the PDIB MCU. These forwarded serial messages are handled by the Atmega 128 using interrupt driven receive buffers. Serial messages sent by PolarisLink are parsed in accordance to the communication protocol and corresponding subroutines are executed.

The firmware on the Atmega 8 handles the control of all digital I/O of the processor based on serial message received from the Atmega 128. Signal lines from Atmega 8 were connected to each user input button of the camera for full accessibility of the camera's features. The firmware also runs a startup sequence every time the camera is turned on. This sequence sets up the camera's manual mode of operation and infinite focus, thereby reducing shutter-lag. After the startup sequence finishes, serial data from the PDIB is available for parsing to control any feature of the camera.

Graphical User Interfaces

Several software packages are needed in order to have full functionality of the UAV. The "Virtual Cockpit" is a GUI that Procerus Technologies[®] provides with their product so the user has access to all functions of the autopilot. In past UAV missions it became evident that payload settings needed to be adjusted while the plane was flying. With the addition of all the on-board electronics, an easy to use GUI was developed to control all the subsystem features of the aircraft to make this platform a truly autonomous mapping system.

The Virtual Cockpit provides the UAV operators with information about various aircraft state data, critical measurements and internal autopilot variables (Figure 5-2). The Virtual Cockpit also has a route planning and real-time UAV trajectory interface. This interface allows the user to setup waypoint entered routes for the UAV to follow as well as displays the current position of the UAV once airborne. The UAV can be instructed to change course, altitude or airspeed at anytime during the flight.

A specialized GUI was developed to enable the user to quickly and easily control functionality of all the secondary systems of the Polaris UAS. A Visual C++[®] user interface, called "PolarisLink" was designed to handle this task (Figure 5-3). The Virtual Cockpit software for the autopilot can communicate bi-directionally over a local Internet Protocol (IP).

Through this network IP, data is shared between Virtual Cockpit and PolarisLink. Virtual Cockpit creates special serial packets based on the custom Polaris communication protocol and appends this data to normally transmitted data over the wireless modem in the Commbot. This data is guaranteed received using an ACK/NACK system by the autopilot and then transmitted out of SERIAL A in a process described earlier. The PolarisLink GUI is very intuitive and easy to use.

By selecting the “Digital Camera Setup” button, an additional window opens up that mimics the back of the Canon A650 digital camera (Figure 5-4). By pressing these buttons, commands are transferred to the camera controller board to mimic these buttons being pressed on the ground. The wireless video displays all the appropriate screens, so the user can change any feature desirable while having visual feedback that it was accepted. After the camera is setup properly, the “GPS Sync Shutter” can be pressed to initiate the automated synchronized image capture process. This process can be turned on and off as desired.

Camera Synchronization

Camera synchronization refers to the time at which remote sensing data is captured relative to the trajectory of the UAV [30]. Most modern GPS receivers have dedicated synchronizing signal called a PPS or pulse-per-second signal, which is based on GPS time and is known to be sufficiently accurate [30]. However, the GPS receiver that was used for this paper and for the last several missions does not generate this pulse. Even if this signal was generated, synchronizing INS state data that is available from autopilot with this pulse is not possible. Therefore a different approach to camera synchronization was implemented.

The autopilot normally wirelessly transmits state data and other autopilot variables approximately every 450 milliseconds, which is sufficient for updating the Virtual Cockpit. Every second a navigation packet (header 248) is sent containing an updated position solution

from the GPS. Since these packets are generated at different times, they cannot be used for synchronization. A special data output mode called “Mixed Telemetry Mode” is capable of outputting data at a 6 Hz rate and contains both attitude and interpolated GPS positions.

When the button on the PolarisLink software entitled “GPS Sync Shutter” is depressed, this special mode is enabled. The firmware in the Atmega128 MCU keeps track of how many times the packet header 29 is sent to the modem for transmitting. As soon as the firmware sees the 14th count of the packet header 29 (~2.33 seconds), it immediately issues a camera shutter command. The time it takes for the camera to receive the “take picture” command is on the order of 15 microseconds and is therefore negligible. The remaining serial data is read into an SRAM buffer in the Atmega 128 until an end of line character is read. As soon as that buffer is full, the data is then sent to the SD card.

It was experimentally determined that the camera takes approximately 1.80 seconds root-mean-square (RMS) to store a full resolution picture onto the SD card. Therefore, triggering a picture capture any faster than this would cause the system to get out of sync as there is no feedback from the camera to the memory module. To be conservative, the system was programmed to command a picture every 2.33 seconds. The slow flying speed of the UAV still provided plenty of overlap amongst consecutive pictures for constructing picture mosaics in the future.

Timing delays in the exposure of the actual photo needed to be considered in the final direct georeferencing solution. Through experimental methods and online sources it was determined that the Canon A650 has an approximate exposure delay of 87 milliseconds. Errors can propagate in both position and orientation of the camera over this time period. An appropriate method for accounting for this offset is to integrate the accelerometers and

gyroscopes over the delay time period and add in this bias to the original position and orientation findings at the time of commanded exposure. However, the autopilot does not provide access to synchronous inertial information, so integration is not an option. Only a two dimensional position correction factor, $\mathbf{r}_{sync\ error}^{world}$ is considered in the georeferencing solution. The third row of 5-1 is fixed because the altitude is assumed constant due to the closed-loop altitude control. The correction factor is similar to dead reckoning, where groundspeed (χ) and heading (ψ) are extrapolated for some time delay to predict a future position. Equation 5-1 shows the 2-D position offset of the camera after τ time. In this case, an 87 millisecond time delay with a ground speed of 14 meters/second would result in a 1.22 meter world position change in the heading of travel.

$$\mathbf{r}_{sync\ error}^{world} = \begin{bmatrix} \Delta East \\ \Delta North \\ 1 \end{bmatrix} = \begin{bmatrix} \chi * \sin(\psi) * \tau \\ \chi * \cos(\psi) * \tau \\ 1 \end{bmatrix} \quad (5-1)$$

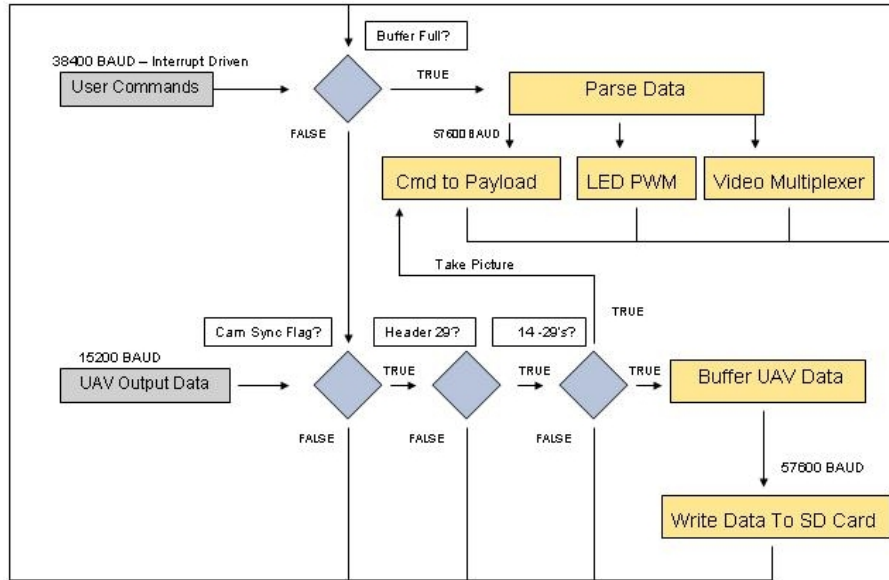


Figure 5-1. Atmega 128 MCU firmware flowchart

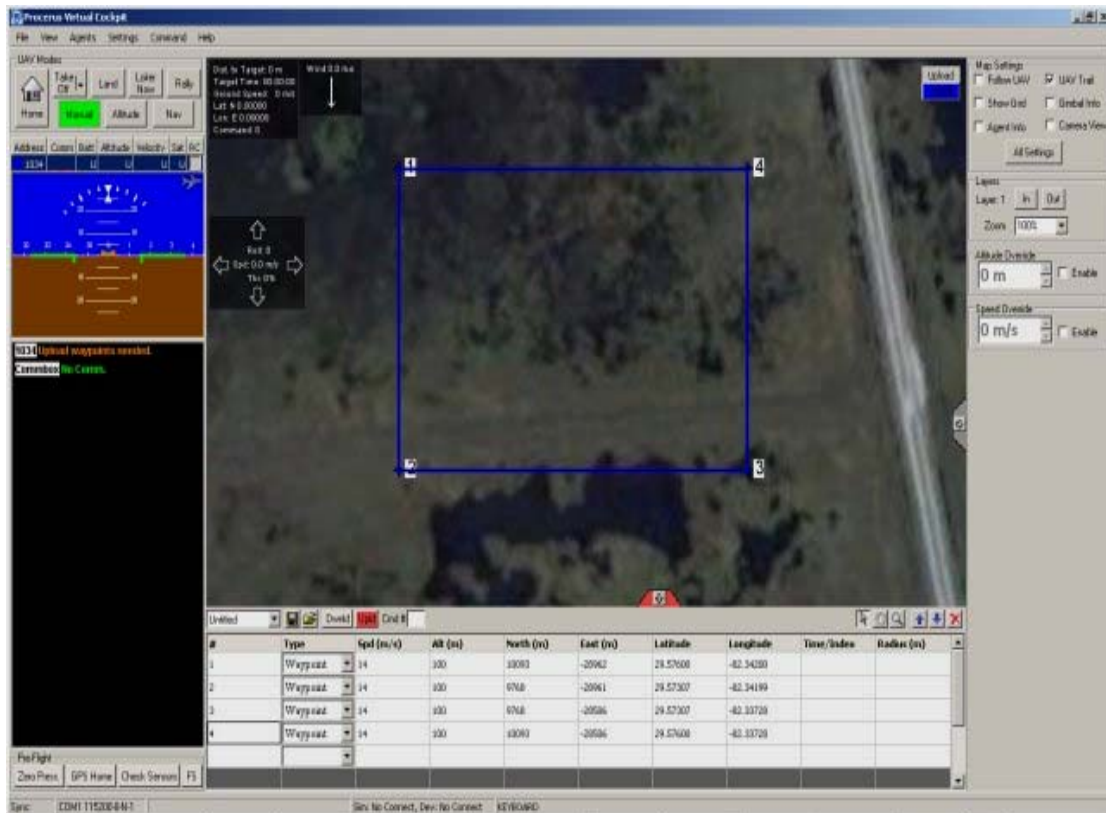


Figure 5-2. Virtual Cockpit software screen shot

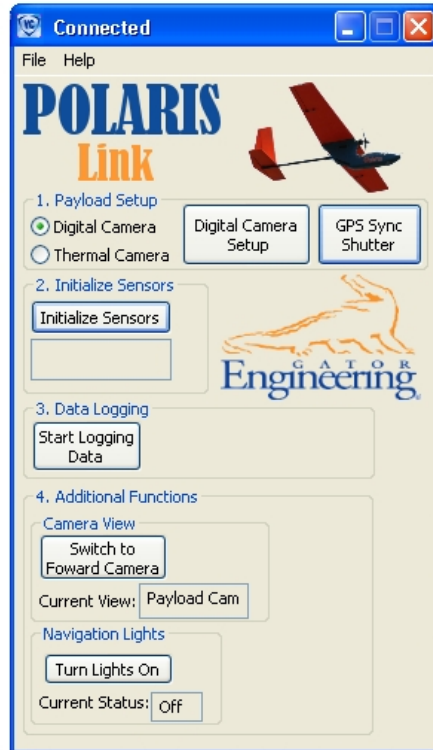


Figure 5-3. PolarisLink software



Figure 5-4. Camera control window

CHAPTER 6 CAMERA CALIBRATION AND INITIALIZATION

Camera Calibration is necessary in order to improve the accuracy of the projective geometry solution for geo-registration. A model of the camera's imaging sensor and optics system as well as the orientation of the sensor at time of exposure is required for accurate direct georeferencing. This process is called solving for the interior and exterior camera parameters. Both of these calibrations are typically done in a lab setting; however, for this application it is not always possible to do so. A fast method was developed for estimating these parameters by using a modified camera calibration toolbox for Matlab[®]. Computing the exterior orientation parameters in order to isolate the boresight of the camera refers to the camera initialization and is usually performed at the flying site before a survey mission.

Calibration Software

Well documented, camera calibration software for Matlab[®] exists that uses images of a known grid size to extract both interior and exterior camera parameters [8]. Functions of this toolbox were modified for automation and field initialization.

The interior calibration parameters include the focal length, scale factor, principle point offset and lens distortion coefficients. A calibration procedure in [8] is used to determine these parameters. Since these parameters are intrinsic to each payload they should only have to be calibrated once. These values are stored in a file called Calib_Results.mat and are saved on the SD[®] card where the UAV state values are written to. Later software assumes that the calibration parameters on this SD[®] card match that of the payload camera. The complete camera model used here includes radial and tangential distortions and can be seen in Equation 6-1. This equation is implemented in the resampling process to undistort the images and to improve the accuracy of the georeferencing solution [33]. In Equations 6-2 through 6-5, \tilde{u}_i and \tilde{v}_i represent

the pixel locations in the image plane of the object coordinates (x_i, y_i, z_i) and a camera focal length, f . Parameters $\delta u_i^{(r)}$ and $\delta v_i^{(r)}$ represent the change in pixel location in the image plane from a radial distortion contribution. Terms k_1, k_2, \dots represent coefficients of radial distortion of the lens and r_i is only a substitution term representing the radial distance of pixel “i” from the principal point. In this case, a fourth order estimation for the radial distortion is used.

Parameters $\delta u_i^{(t)}$ and $\delta v_i^{(t)}$ represent pixel offsets in the image plane due to tangential distortions. Terms p_1, p_2 are coefficients of tangential distortion. Parameters u_i and v_i represent the actual location of object points (x_i, y_i, z_i) in the image plane. Constants D_u and D_v are conversion factors that are necessary to transform metric units to pixels. These are typically taken from the image sensor datasheets. The term S_u is a scale factor that is adjusted in the iterative solution to solve for lens distortions unknowns. Typically, S_u is close to 1. Terms u_0 and v_0 are the coordinates of the image center, also known as the principal point.

$$\begin{bmatrix} \tilde{u}_i \\ \tilde{v}_i \end{bmatrix} = \frac{f}{z_i} \begin{bmatrix} x_i \\ y_i \end{bmatrix} \quad (6-1)$$

$$\begin{bmatrix} \delta u_i^{(r)} \\ \delta v_i^{(r)} \end{bmatrix} = \begin{bmatrix} \tilde{u}_i (k_1 r_i^2 + k_2 r_i^4 + \dots) \\ \tilde{v}_i (k_1 r_i^2 + k_2 r_i^4 + \dots) \end{bmatrix} \quad (6-2)$$

$$\begin{bmatrix} \delta u_i^{(t)} \\ \delta v_i^{(t)} \end{bmatrix} = \begin{bmatrix} 2p_1 \tilde{u}_i \tilde{v}_i + p_2 (r_i^2 + 2\tilde{u}_i^2) \\ 2p_2 \tilde{u}_i \tilde{v}_i + p_1 (r_i^2 + 2\tilde{v}_i^2) \end{bmatrix} \quad (6-3)$$

$$\begin{bmatrix} u_i \\ v_i \end{bmatrix} = \begin{bmatrix} D_u s_u (\tilde{u}_i + \delta u_i^{(r)} + \delta u_i^{(t)}) \\ D_v (\tilde{v}_i + \delta v_i^{(r)} + \delta v_i^{(t)}) \end{bmatrix} + \begin{bmatrix} u_0 \\ v_0 \end{bmatrix} \quad (6-4)$$

$$r_i = \sqrt{\tilde{u}_i^2 + \tilde{v}_i^2} \quad (6-5)$$

The following describes the process used to perform a self-calibration to determine interior camera model parameters. For calibrating the Canon A650 sensor in the Polaris, the camera was left in the protective carbon box and installed into the fuselage; the wings were left off and a battery was installed. A grid of black and white squares was printed out and mounted to a flat sheet of Plexiglas[®]; taught as possible. The squares were measured with a micrometer and determined to be 28.45 mm per side. Using the wireless video transmission and the PolarisLink camera control window, a series of eleven pictures were taken at varying heights and orientations about the calibration grid. The images were taken at a 640 x 480 resolution because the camera calibration toolbox has to read in all the images in order to start the calibration process; this is very RAM intensive. The reduced resolution has to be taken into account for later for un-distorting high resolution images. Images were transferred to a computer working directory for calibration via the PolarisView GUI. The calibration photos can be seen in Figure 6-1. (It should be noted that near the edges there is photo occlusion from the UAV fuselage.)

The software uses grid corner intersection detection for control points. Internal intersections of other grid points can automatically be determined if the four corners of the enclosed box is selected. The software can also count the total number of squares in the picture, but if the software guess is wrong, then the user can enter it manually. The order that the user clicks is important, therefore numbers were added to the actual calibration grid so that in the calibration software, the corner numbers are visible and provide a guide in which corner to start

with. The corner intersection must start internal to the grid, not on the outer most squares. The first selected corner will dictate the grids origin, the second point establishes a line connecting the first and second points. This is the Y-axis of the photo. All four corners should be selected in clockwise fashion. The right-hand rule dictates the Z-axis of the checkerboard. The software produces predicted edge corners for the center pixels. If they are satisfactory, the user can continue, else an initial radial distortion factor is asked to be input. In the case of the Canon A650, an initial estimate of -0.25 was required in order to get central edge detection to appear correct (Figure 6-2). The size of the actual squares is input next. After all images are brought in through this fashion, the initial calibration can commence. There are two procedures used to calculate interior parameters here. The first is a closed form solution that is not based on any lens distortions. The second procedure involves a non-linear optimization that minimizes the reprojection errors on to the photo, namely 9 degrees of freedom in the intrinsic parameters [33]. The radial and tangential effects of the lens can be seen in Figure 6-3. A complete distortion model and interior calibration parameters including uncertainties can be seen in Figure 6-4. The complete model combines the effects of tangential and radial distortion in a single plot, effectively showing true pixel location due to lens distortion. The coefficients shown in Figure 6-4 can be substituted in to Equation 6-4 to realize the camera model for the Canon A650. It is obvious that this particular camera suffers from a decentering error, meaning that the effective center of the photo is different from the geometric center [33]. Now that the interior parameters are realized, images can be resampled in order to take into account lens distortions (Figure 6-5).

The software also has the ability to solve for exterior camera parameters. These parameters give the relative location of the camera versus the grid and consist of a translation vector and a rotation matrix. The software uses the grid corner locations relative to each other to

determine the roll, pitch and yaw of the camera at the time of exposure. Figure 6-6 shows the orientation of the UAV fuselage when the calibration images were taken. However, these orientations are meaningless for the moment. The same procedure to find the exterior parameters is used in field initialization, only the results will give the boresight or relative orientation of the camera versus the IMU.

Initialization Jig

A method for determining the payload's boresight at the field was developed to calibrate the exterior parameters quickly and easily before flight. Theoretically, if the camera was never remounted before the previous flight, this procedure could be skipped to save time.

Since direct georeferencing will be accomplished using only the measurements from the UAV's INS, it is necessary that the boresight misalignment be represented relative the measurements of this INS. The Polaris requires an inertial initialization procedure in which the trimmed flying condition is specified to the INS by holding the aircraft level. This level calibrated condition is what the autopilot's closed-loop control tries to regulate about during straight flight paths. Figure 4-6 shows these control loops. The concept of estimating the exterior orientation parameters consists of initializing the autopilot and then taking a picture of the calibration grid. A bubble level was used on the aircraft and on the calibration grid to ensure that both platforms were orthogonal to each other. The resulting exterior parameters represent purely the boresight misalignment of the camera (image frame) relative to the IMU. A special initialization jig was designed to facilitate this procedure easily.

The initialization jig consists of a heavy-duty fluid head tri-pod with a fuselage cradle mounted on top. The cradle has a hole cut out of the bottom for the payload camera to view through. The cradle is lined with a mid-density foam to secure the fuselage in place. Once the plane is placed in the cradle, a 2-axis bubble level is placed on a flat portion of the fuselage. The

tripod is manipulated as to level the aircraft indicated by the bubble level. The tri-pod is then rotated to north using a hand held compass.

Using the wireless video from the payload camera, the calibration grid is then placed below the payload hole enough to view most of the grid in the field of view of the camera. A platform of any type can be placed underneath the Plexiglas[®] calibration grid apparatus. The grid is then leveled and twisted toward north using the 2-axis bubble level and compass respectively. Figure 6-7 shows the initialization jig assembly and 2-axis bubble leveling.

The Polaris Link software is used to run the initialization procedure. First, the Polaris' main power is turned on and left on for about 5 minutes as to let the avionics come to a steady state temperature. Then, the "Initialize Sensors" button is used to initialize the INS to a level flying condition. Once all axes of the aircraft states read zero on the Virtual Cockpit, the "GPS Sync Shutter" button can be pressed. After a few second delay due to the memory card writer initializing, a picture will be taken of the calibration grid. The wireless video will confirm this step. The "GPS Sync Shutter" can now be turned off and is ready for a survey mission. The Polaris now has the data needed to calculate the boresight misalignment for direct georeferencing during post-processing.

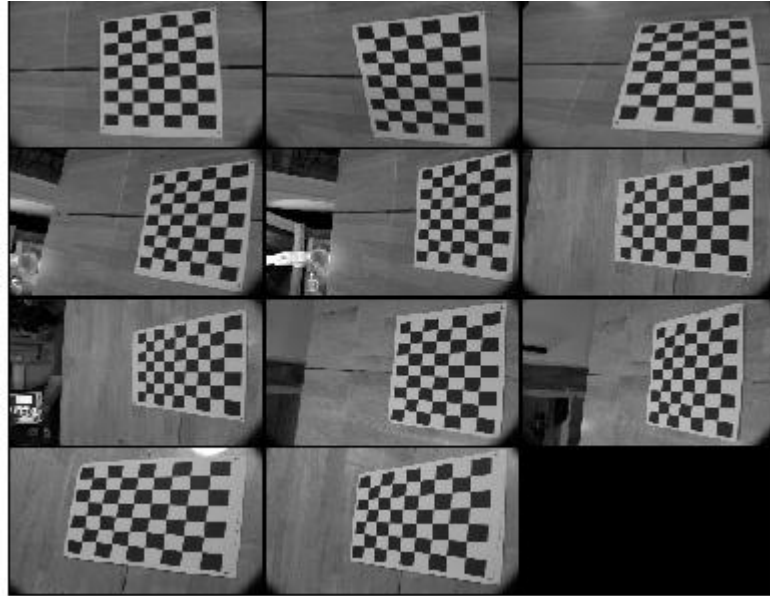


Figure 6-1. Images used for camera calibration. Original images are in color, but calibration software resamples to black and white.

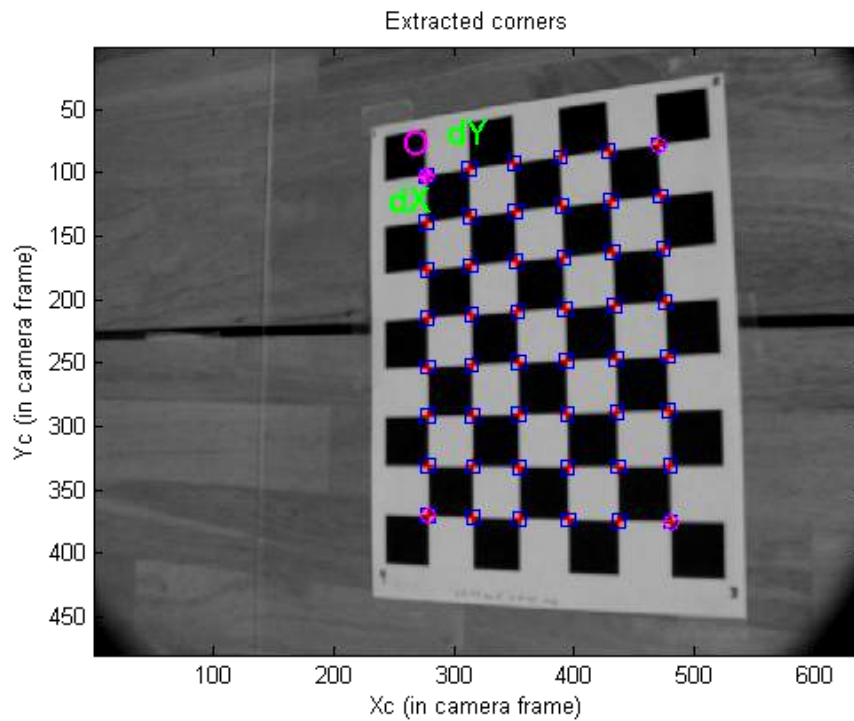


Figure 6-2. Internal grid intersection points are based on square sizes and initial lens distortion coefficient k_c .

A

B

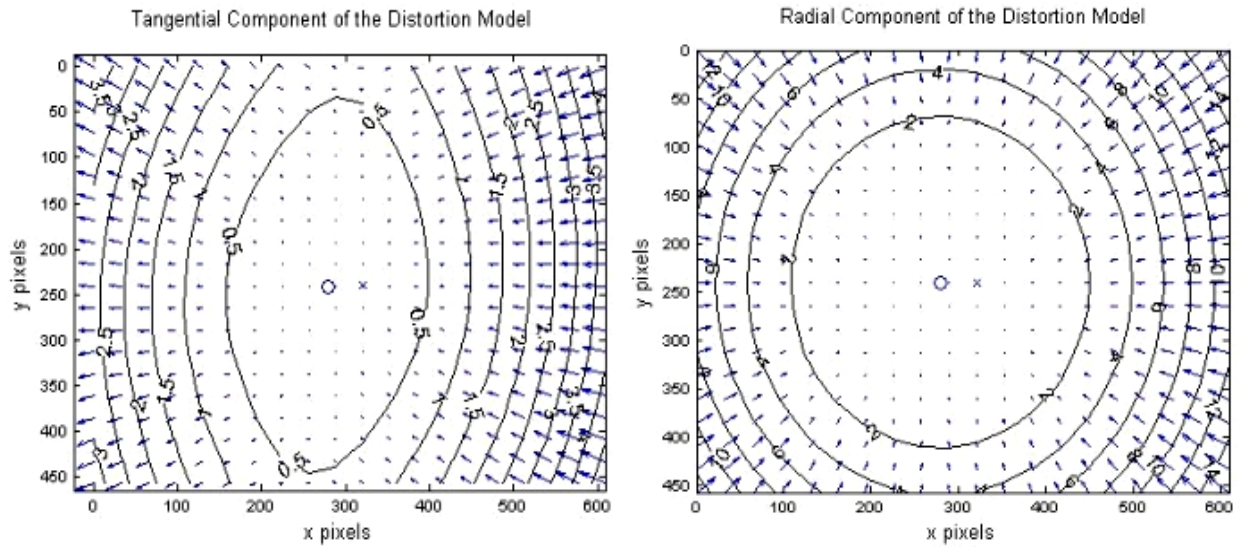


Figure 6-3. Lens distortion model of Canon A650. A) Tangential lens distortion. B) Radial lens distortion

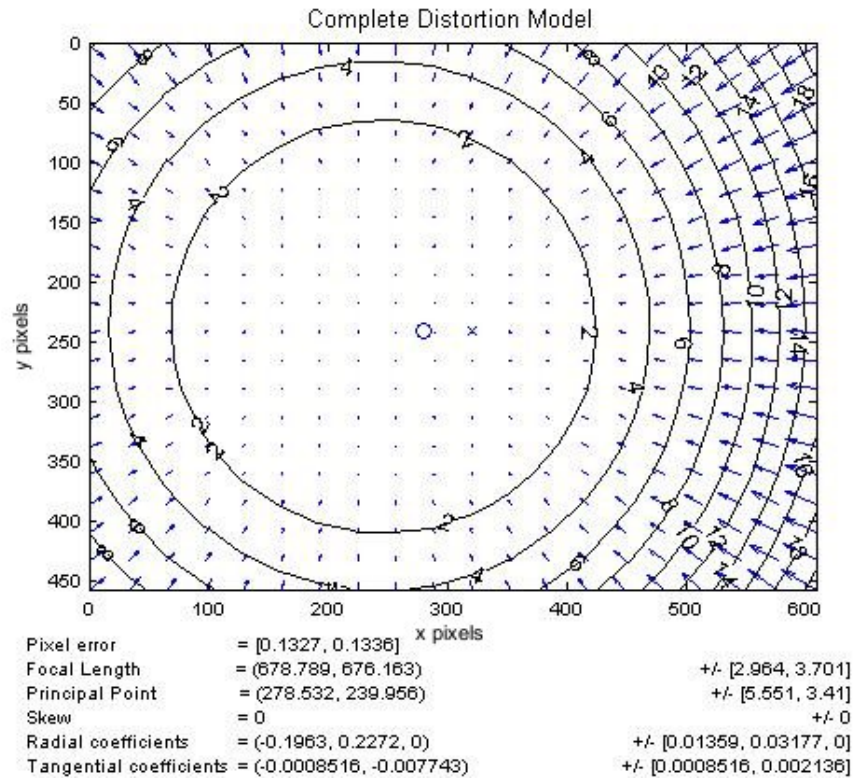


Figure 6-4. Complete lens distortion model. Radial and tangential effects have been combined into a complete model.

A

B

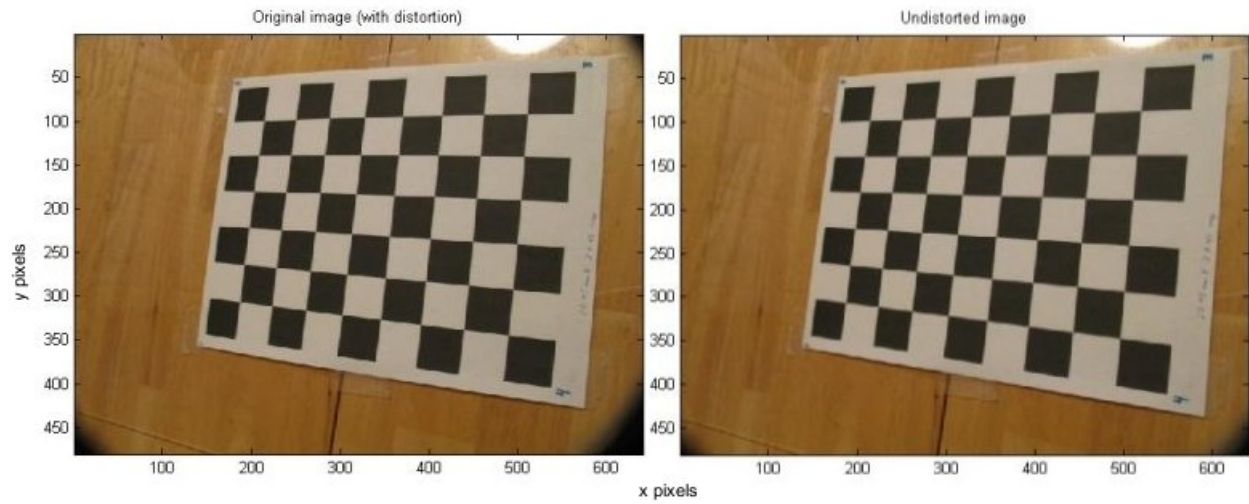


Figure 6-5. Comparison of distorted picture based on lens parameters. A) Original distorted picture B) Undistorted picture

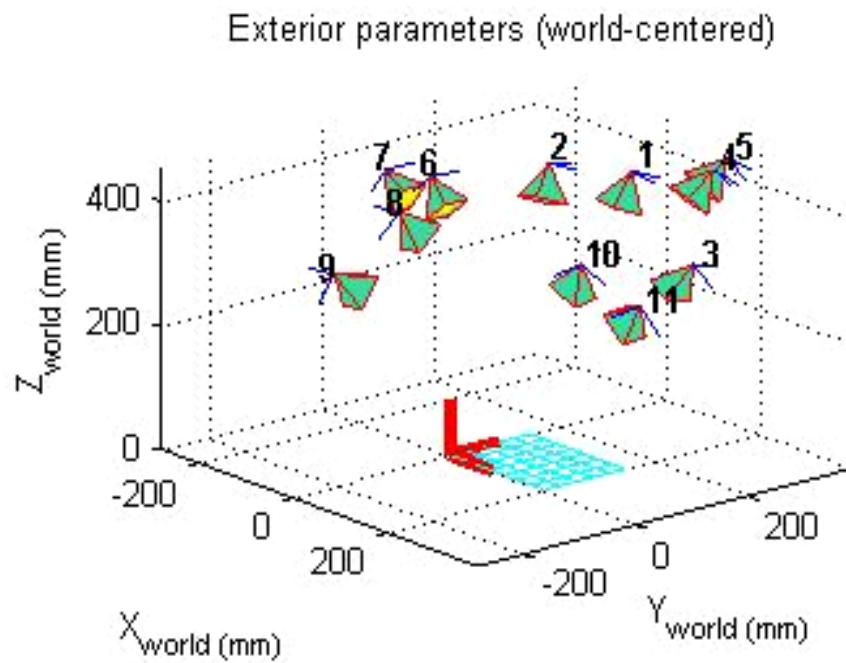


Figure 6-6. Exterior camera parameters for indoor calibration.

A

B



Figure 6-7. Field initialization process for determining camera boresight misalignment A) Initialization Jig used for extracting exterior calibration parameters. B) Bubble leveling technique used to ensure orthogonality between calibration grid and UAV.

CHAPTER 7 RAPID MAPPING

Synchronized imagery, aircraft orientation and camera calibration data are stored on two independent SD[®] cards aboard the Polaris UAV. A picture number on both cards is the common link between both the set of images on one card and the corresponding data on the other. Rapid mapping of the imagery collected from the Polaris is the primary goal of this system. Often, the UAV either flies over terrain that is impossible to set out ground control points on or has too many similar features to rely on an auto-detection algorithm to generate control points. Therefore, a direct georeferencing method was used to compute mapping coordinates and georegister the images. There was no COTS software that existed that could handle the output format of the Polaris in a rapid batch fashion, so specialized software was developed to promote user-friendly, autonomous processing. The software was developed in Matlab[®] and written general enough to be easily adapted to future UAV platforms.

Coordinate Frames

In order to properly locate a target on the ground or realize photographic capture boundaries, several coordinate frames must be established. There were three coordinate frames necessary in the process of overlaying geo-registered images into Google Earth[®], namely the body frame, image frame and the world frame. The image frame was chosen to be the computational frame and is where all aircraft coordinate frames are transformed to for spatial analysis and direct georeferencing. The world frame is where projected ground coordinates exist. All axes naming conventions were assigned arbitrarily in a right-handed fashion in order to resolve any inconsistencies in motion axes amongst aeronautical engineering, geodetic science and traditional photogrammetry.

The world frame is defined with respect to the reference ellipsoid. The reference ellipsoid is a simplified model of the shape of the earth [39]. It can be expressed by simple equations in which a typical ellipsoid is flattened at the poles; there exists a semi-major axis (a) and a semi-minor axis (b) [39]. The GPS receiver used on the Polaris UAV uses the WGS84 datum values for (a) and (b) [40] (Table 7-1). The z-axis of the world frame is orthogonal to the reference ellipsoid, the y-axis is always aligned with geodetic north and the x-axis is a cross product of the y and z axes to form a right-handed coordinate system [39]. In other words, the world frame is tangent to the reference ellipsoid; the x-axis points to the east, the y-axis points toward north and the z-axis is orthogonal to the earth's surface (also known as East-North-Up system). There are two instances of the world frame used here and are identical in a 2-D sense; the first is fixed to the ground and the other is a distance h off the ground, centered at Polaris' GPS receiver. A position vector in the world frame attached to the UAV is shown in Equation 7-1.

$$\mathbf{r}_{UAV}^{world} = \begin{bmatrix} x^{world} \\ y^{world} \\ h \end{bmatrix} \quad (7-1)$$

The height h is the combination of the UAV's altitude, alt , measured by the barometric (static) pressure sensor on the autopilot and the difference in spacing between the autopilot and GPS receiver. The GPS output altitude was not used in the direct georeferencing solution. The autopilot in the Polaris UAV uses geodetic latitude (Φ) and longitude (λ) for 2-D navigation (Figure 7-1). However, it was necessary for the location of the aircraft to be represented in units that were consistent amongst other coordinate systems. That is, all units of spatial measure are represented in meters. Latitude and longitude data from the aircraft was therefore converted to UTM coordinates during post-processing. The PolarisView software uses a UTM (Universal

Transverse Mecator) Cartesian coordinate system that complements the make-up of a digital image.

The body frame is an orthogonal frame whose origin and orientation is arbitrary [39]. In this case, the body frame's origin is fixed to the center of the IMU (inertial measurement unit) on the autopilot and is where the physical inertial measurements are made. The location of the IMU was basically on the center-of-mass of the aircraft. The coordinate system within the body frame was defined where the x-axis is out the right wing, the y-axis is out the nose and the z-axis is out the top of the UAV (Figure 7-1). A position vector in the body frame is given in 7-2.

$$\mathbf{r}^{body} = \begin{bmatrix} x^{body} \\ y^{body} \\ z^{body} \end{bmatrix} \quad (7-2)$$

Any rotation of the body frame axes relative to the initialized level condition with respect to the world frame describes the aircraft's attitude. The angles by which the attitude is comprised are called Euler angles [41]. The pitch (θ) angle of the UAV is determined by the amount of rotation about the x-axis where a positive pitch describes a nose up condition. The roll (ϕ) angle is the measure of rotation about the y-axis where a right wing down condition describes a positive roll. The yaw (ψ) angle is a measure of rotation about the z-axis where a positive yaw rotates the nose in a counter-clockwise direction. However, heading used for navigation is measured in a clockwise fashion; therefore a sign change was implemented in the PolarisView software.

The image frame is a coordinate frame in which the perspective center, P.C. is the origin. The naming convention of the axes stayed consistent with the other previous frames to avoid intermediate transformations amongst coordinate frames. The x-axis is defined out of the top of

the camera, the y-axis is defined out of the left side of the camera and the z-axis is defined out the opposite direction of the lens (Figure 7-1 & Figure 7-2). A position vector in the image frame can be seen in 7-3.

$$\mathbf{r}^{image} = \begin{bmatrix} x^{image} \\ y^{image} \\ z^{image} \end{bmatrix} \quad (7-3)$$

The world frame fixed to the ground is where resulting direct georeferenced coordinates lie. The estimated ground coordinates dictated how the image was to be geo-registered. The world frame fixed to the ground is also expressed in UTM's. Polaris' 2-D position at any point in time is common among both instances of the world frame. The origin of the UTM projection lies at the central meridian and the equator's intersection [42]. A position vector in the mapping frame is shown in 7-4. The x^{world} coordinate expresses distance east of the origin and the y^{world} coordinate expresses distances north of the origin while the z^{world} coordinate expresses the distance above the reference ellipsoid. For flat terrain testing that was conducted here, z^{world} was fixed to zero.

$$\mathbf{r}_{ground}^{world} = \begin{bmatrix} x^{world} \\ y^{world} \\ z^{world} \end{bmatrix} \quad (7-4)$$

Direct Georeferencing

Traditional image-to-ground georeferencing strategies involve the inclusion of ground control points that have to be manually determined from land based GPS or similar spatial measuring tool. Often, areas in which UAVs are operated have indistinguishable ground

features, eliminating the possibility of using existing objects as GCPs. Therefore, in order to have ground control in images taken by the Polaris, manual ground-based objects would have to be laid. Small footprint photographs taken by the Polaris would require a large number of these ground control points spread. This process would be very time and labor consuming and defies the quick-to-fly ability of the Polaris. Consequently, the concept of direct georeferencing was implemented to estimate such ground points. Due to the proprietary nature of the autopilot and wireless bandwidth constraints, the direct georeferenced solution is based solely on the discrete aircraft state parameters at the time of exposure.

The process of direct georeferencing transforms image coordinates into ground world coordinates through the location and orientation of the camera at the time of exposure. Using the developed camera calibration process, synchronization error, and GPS/strap-down INS, these parameters can be computed. The mathematical expression for the camera's positioning can be modeled as a spherical joint robot with a three degree-of-freedom end-effector, much like mechanisms described in [43]. In order to properly assign the position and orientation parameters of the camera for direct georeferencing, the world frame attached to the UAV and the body frame had to be transformed into the image frame. This was accomplished by a series of rigid body rotations, and link offsets.

The IMU was treated as the UAV's global origin. Distances to the image frame origin (perspective center, P.C.) and GPS receiver were measured relative to the IMU. In addition, the boresight of the camera had to be included as a rotational bias that impacted aircraft Euler angle measurements with respect to the image frame. The \mathbf{r}_{GPS}^{body} variable was introduced to represent the spatial difference between the GPS receiver and the IMU in body frame coordinates (7-6). The $\mathbf{r}_{P.C.}^{body}$ parameter describes the location of the camera versus the IMU (7-7). The Euler

angles of the aircraft were expressed as a DCM (direction cosine matrix) and can be seen in 7-8.

The \mathbb{R}_x^y symbol represents a 3x3 rotation matrix which relates the orientation of one coordinate frame to another. The subscript x represents the original coordinate frame and y represents the subsequent coordinate frame. The rotation matrix $\mathbb{R}_{body}^{world}$ was constructed using methods outlined in [43]. In 7-8, an s was used in place of sine and a c was used in place of cosine. All sequence of rotations used for photogrammetric analysis were X,Y,Z which corresponds to pitch (θ), roll (ϕ) and yaw (ψ) in Euler angles. The 3-D estimate of the location of the image plane origin in world coordinates measured from the body frame origin can be seen in 7-9.

$$h = alt + z_{GPS}^{body} \quad (7-5)$$

$$\mathbf{r}_{GPS}^{body} = \begin{bmatrix} x^{body} \\ y^{body} \\ z^{body} \end{bmatrix} \quad (7-6)$$

$$\mathbf{r}_{P.C.}^{body} = \begin{bmatrix} x^{body} \\ y^{body} \\ z^{body} \end{bmatrix} \quad (7-7)$$

$$\mathbb{R}_{body}^{world} = \begin{bmatrix} c\phi c\psi & c\phi s\psi & -s\phi \\ -c\theta s\psi + s\theta s\phi c\psi & c\theta c\psi + s\theta s\phi s\psi & s\theta c\phi \\ s\theta s\psi + c\theta s\phi c\psi & s\theta c\psi + c\theta s\phi s\psi & c\theta c\phi \end{bmatrix} \quad (7-8)$$

$$\mathbf{r}_{P.C.}^{world} = \left[\mathbf{r}_{GPS}^{world} + \mathbf{r}_{syncerror}^{world} \right] + \mathbb{R}_{image}^{world} \mathbb{R}_{body}^{image} \left[\mathbf{r}_{P.C.}^{body} - \mathbf{r}_{GPS}^{body} \right] \quad (7-9)$$

After the 3-D position of the camera was realized, the effective orientation of the camera was determined. In the initialization section, a method for determining the boresight of the camera was devised. This rotational bias was combined with the aircraft's attitude to render the image frame's actual orientation relative to the world frame at the time of picture capture. The rotation matrix that describes the body frame axes relative the image frame (camera boresight) is similar to 7-8, except x represents a rotation about the body frame x-axis, y about the y-axis and z about the z-axis (7-10). A matrix multiplication of the Euler angle DCM and the camera's boresight DCM provided the correct orientation of the image plane (7-11).

$$\mathbb{R}_{image}^{body} = \begin{bmatrix} cy \ cz & cy \ sz & -sy \\ -cx \ sz + sx \ sy \ cz & cx \ cz + sx \ sy \ sz & sx \ cy \\ sx \ sz + cx \ sy \ cz & sx \ cz + cx \ sy \ sz & cx \ cy \end{bmatrix} \quad (7-10)$$

$$\mathbb{R}_{image}^{world} = \mathbb{R}_{body}^{world} * \mathbb{R}_{image}^{body} \quad (7-11)$$

Once the position, $\mathbf{r}_{P.C.}^{world}$, and orientation, $\mathbb{R}_{image}^{body}$, of the camera sensor were established, ray projection intersections from the image frame to the world frame could be computed. These intersections in world coordinates are the estimated captured coordinates of the digital image. The assumption of a flat-earth model was made for photogrammetric analysis in the PolarisView software.

Direct Linear Transformation Method

A photograph contains three dimensional features in a two dimensional space. In order to locate desired features in the photograph, a mathematical model describing the relationship between the photo and captured space is conceived. Many different models for this exist, however, the direct linear transformation (DLT) method is selected, here.

The DLT method uses an ideal pinhole model of the camera, where the image plane is offset in the negative z direction a distance, f , known as the focal length, away from the camera sensor's origin [32]. A collinearity condition in analytical photogrammetry states that at the time of exposure, any object point on the image plane and its photo image on the earth all lie along a straight line in three-dimensional space [44]. The image plane is devised of pixels in an x,y tabled fashion and has a central pixel location called the principal point [1]. A vector originating from the pinhole to each individual pixel in the image plane describes the composition of the vector that continues through the image plane to the earth's surface (Figure 7-3). One mathematical expression for the collinearity equations is shown in 7-12, which describes the vector from the pinhole to a specific point on the image plane [7].

$$x_i = x_0 - f \left[\frac{m_{11}(x_i^{world} - x_{P.C.}^{world}) + m_{12}(y_i^{world} - y_{P.C.}^{world}) + m_{13}(z_i^{world} - z_{P.C.}^{world})}{m_{31}(x_i^{world} - x_{P.C.}^{world}) + m_{32}(y_i^{world} - y_{P.C.}^{world}) + m_{33}(z_i^{world} - z_{P.C.}^{world})} \right] \quad (7-12)$$

$$y_i = y_0 - f \left[\frac{m_{21}(x_i^{world} - x_{P.C.}^{world}) + m_{22}(y_i^{world} - y_{P.C.}^{world}) + m_{23}(z_i^{world} - z_{P.C.}^{world})}{m_{31}(x_i^{world} - x_{P.C.}^{world}) + m_{32}(y_i^{world} - y_{P.C.}^{world}) + m_{33}(z_i^{world} - z_{P.C.}^{world})} \right]$$

The terms x_i and y_i refer to image plane coordinates of a desired point i in world coordinates. The coordinates x_0 and y_0 refer to the location of the principle point of the image plane. The f parameter is again the focal length of the camera. The m_{xx} terms correspond to the elements of the $\mathbb{R}_{image}^{body}$ matrix given in a row/column subscript. The $x_{P.C.}^{world}$, $y_{P.C.}^{world}$ and $z_{P.C.}^{world}$ terms have all been defined previously as origin of the image frame in world coordinates. Coordinates x_i^{world} , y_i^{world} and z_i^{world} are the location of the ground-based object, they represent the estimated ground coordinates of point i in the world frame. Since the PolarisView software assumes the

ground flat, z_i^{world} is equal to zero. Equation 7-13 shows the general form of the direct georeferencing equation where \mathbf{r}_j^{world} is the estimated world coordinates of an object j from the image frame projection and world frame intersection. The s term is a scale factor that is based on ground level elevation; in this case it is fixed because the flat-earth model is being used.

$$\mathbf{r}_j^{world} = s * \mathbb{R} \begin{matrix} world & image \\ image & j \end{matrix} \mathbf{r}_j + \mathbf{r}_{P.C.}^{world} \quad (7-13)$$

Photo Geo-Registration

At the time of exposure, the UAV is not orthogonal to the ground which affects the image area coverage of the photograph. The geometry of the resulting image undergoes a projective transformation that distorts the actual area coverage and therefore the land area each pixel contains. Therefore, the digital images are resampled based on interior camera parameters and the collinearity equations. The resulting physical image will appear distorted; however, the land area that each pixel contains will be approximately equal allowing for the image to be registered into a defined mapping space.

The algorithm implemented for resampling the images into a projective space moves the discrete pixel element in the image plane space to a blank world space dictated by the projective transformation. The resampling process employs a bicubic interpolation that results in a smoother color transition and less artifacts over the nearest-neighbor or bilinear interpolation. The geo-registered image corner points are georeferenced to a Cartesian Transverse Mercator Projection using the WGS84 datum and UTMs. Blank black pixels are used to keep rectangularity of the output image in order to geo-register image into Google Earth. The corner coordinates are converted to geodetic latitude and longitude for importation into Google Earth[®] via a KML file. Figure 7-4 shows several examples transformations.

PolarisView Graphical User Interface

After previous missions, each photograph had to be manually adjusted and registered into Google Earth[®] for analysis. This was very time consuming and took as long as two weeks to attempt to fit the photographs. Software was written to automate the geo-rectification process and can output images to Google Earth[®] as soon as they image is resampled. Various options in software allow filtering of selected images in a data set. Geo-registered images and linking KML files are transferred to a common directory automatically to be viewed in various GIS tool-sets. Google Earth[®] was chosen in this case because the software automatically deals with image pyramiding, a scheme by which the resolution of the photos are increased or decreased depending on zoom height.

Using a simple SD[®] to USB adapter, data can be moved seamlessly to appropriate hierarchal directories for decompiling and mapping. After the transfer of the original data, PolarisView automatically formats the SD[®] cards and recopies calibration files back to the SD[®] card for another flight. A brief overview of the software and a typical mapping process can be seen below.

The user has to complete several steps in sequence in order to output “map-able” imagery. First, the camera’s relative position and orientation must be determined. A separate window is launched that allows the user to input locations of the camera and GPS receiver relative to the autopilot’s IMU so all coordinate frames can be transformed into the camera frame (Figure 7-6). PolarisView uses methods of exterior camera parameter extraction seen in Chapter 6 to calculate the boresight misalignment (Figure 7-7). All intrinsic and extrinsic camera parameters are saved to a text file so a recalibration is not necessary the next flight unless the camera payload is removed. The horizontal (cross-track) and vertical (parallel-track) field of view are calculated and also stored on the memory card. Next, the ASCII represented binary aircraft state data in

IEEE754 floating-point format must be parsed and converted to decimal form. The “Parse UAV Data” button runs all the necessary functions to handle this. PolarisView generates a text file that contains all converted elements in a tab-delimited format for separate analysis.

The user has two options at this point; either start output mapping or plot estimated image area coverage. The latter is recommended first in case there are areas that is not of interest from the flight. The area coverage assessment places translucent yellow polygons over Google Earth rendered maps outlining predicted area covered during that particular photograph (Figure 7-8). The user can “filter” the data by limiting roll and pitch angles or by limiting the distance between nadir points of photographs. This separate filtered data is also made available in a text file and linked in a KML to the polygon overlays. A checkbox entitled “Output to Google Earth Realtime” generates immediate polygon overlays or places completed rectified image on Google Earth. Otherwise, the user could launch the KML file associated with that data set run. Finally, the “Generate Rectified Photos” button starts the original image to digitally rectified directly georeferenced image process. The option to reduce the resolution is provided to accelerate the mapping process. A status box was provided to show completion of the data set. The process can be stopped at anytime by checking the stop box; the process will suspend after the current picture is finished. All overlays KMLs and data text files are stored in the output directory chosen by the user. All rectified imagery and image KMLs are stored in the “output directory\Photos” directory.

Table 7-1. The WGS84 reference ellipsoid values

Parameter	Measure
Semi-Major Axis (a)	6378137.0 meters
Semi-Minor Axis (b)	6356752.3142 meters
Eccentricity (e)	0.081819191

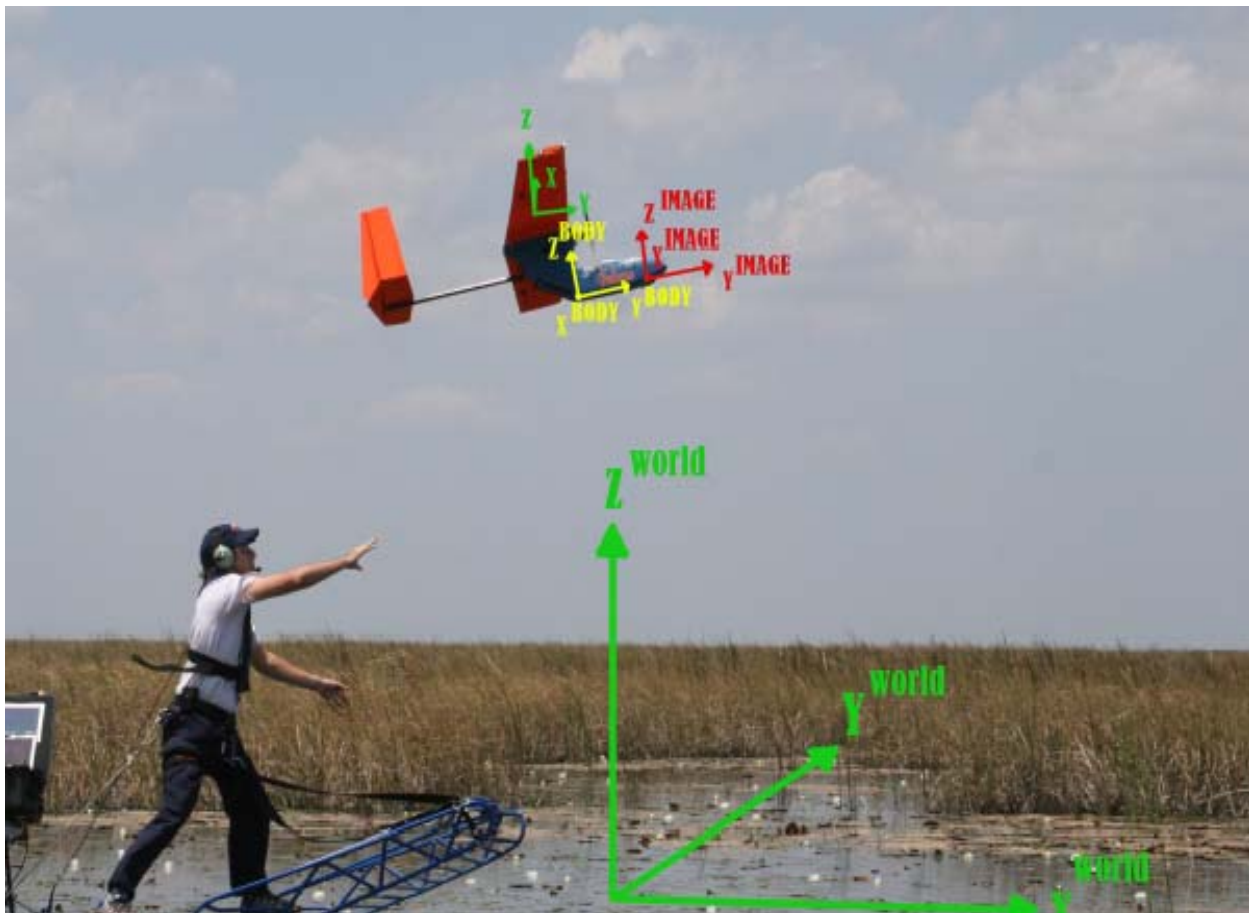


Figure 7-1. Definition of coordinate frames used in direct georeferencing

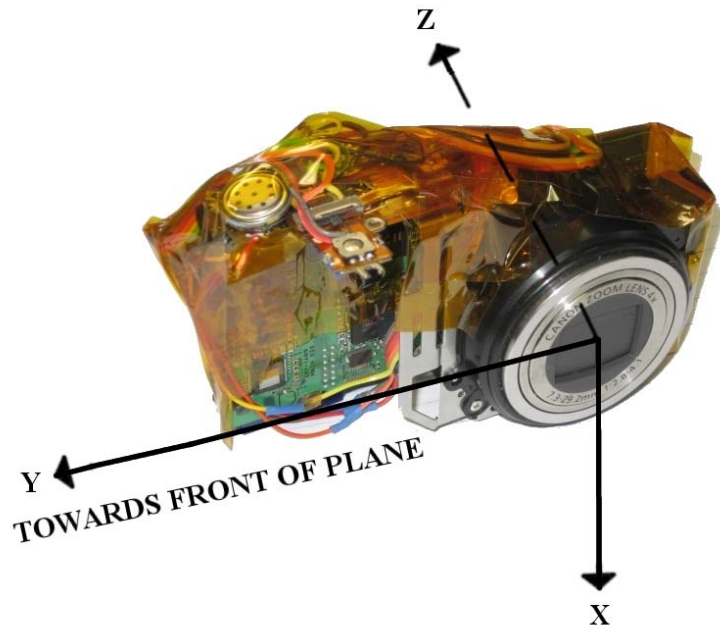


Figure 7-2. Definition of Image Frame Coordinate System

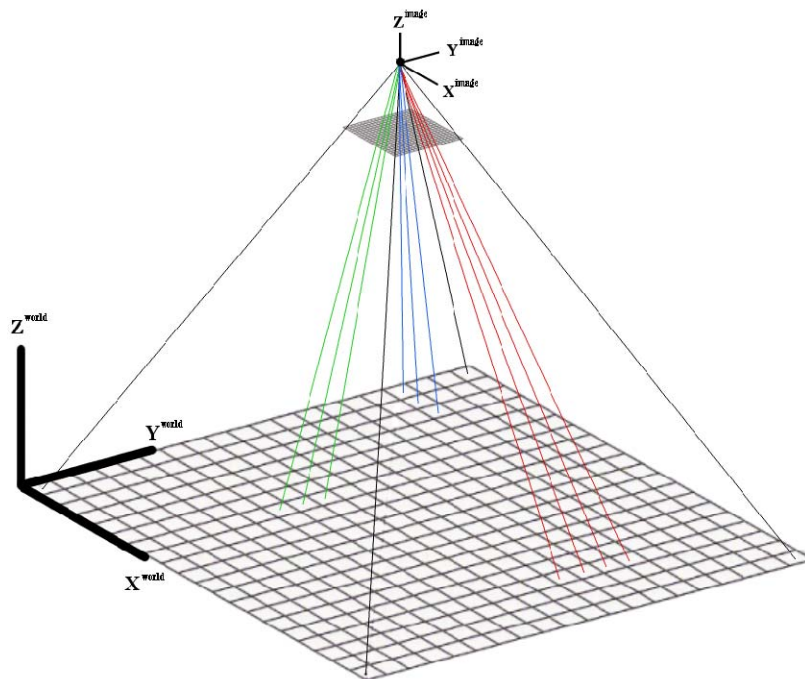


Figure 7-3. Example of DLT projections from camera frame origin through image plane to ground coordinates in mapping frame satisfying collinearity conditions.

A

B

C

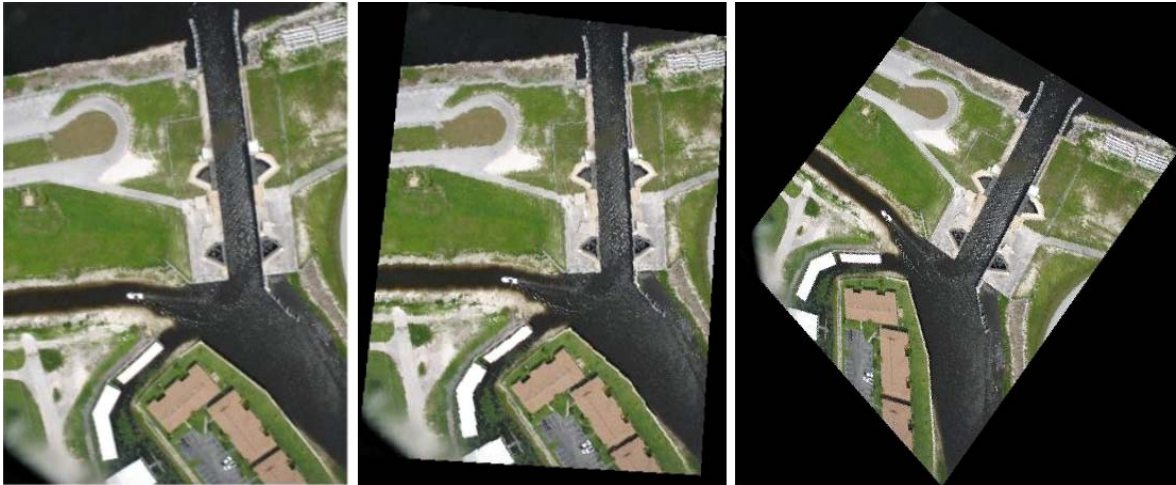


Figure 7-4. Digitally Geo-registered Photos. All photos were taken at approximately 150 meter altitude .A)Original image taken over a levee lock system in South Florida. B) Distortions with 3 deegs of roll, -4 deegs of pitch and 5 deegs of yaw. C) Distortions -10 deegs roll, -10 deeg pitch and 35 deeg yaw.

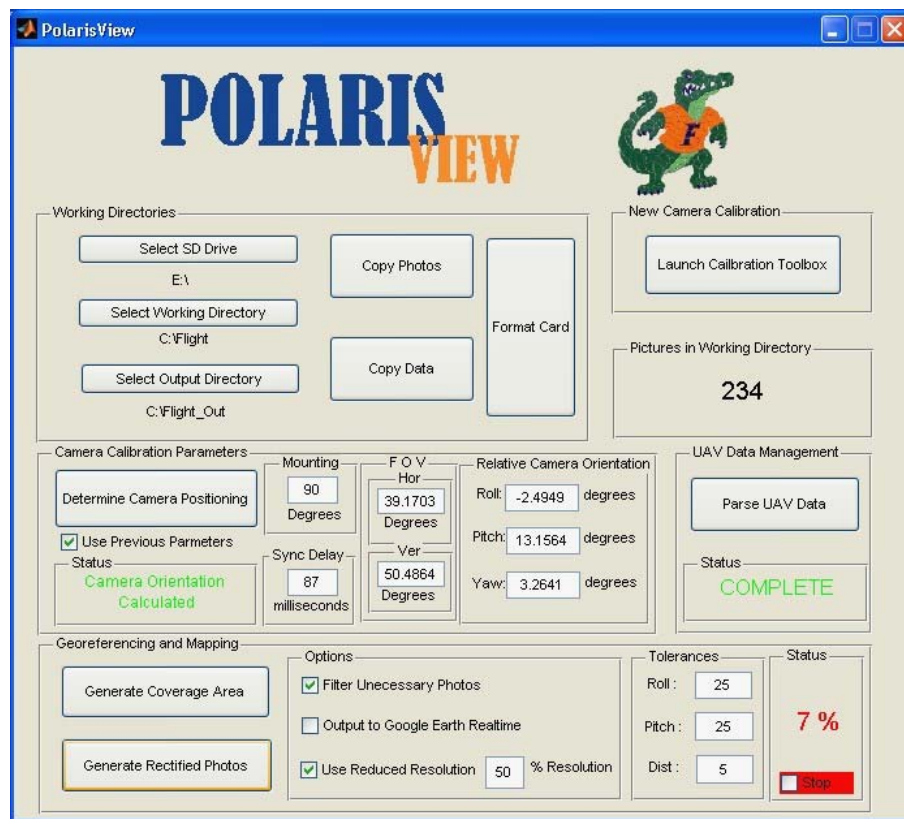


Figure 7-5. PolarisView GUI software package

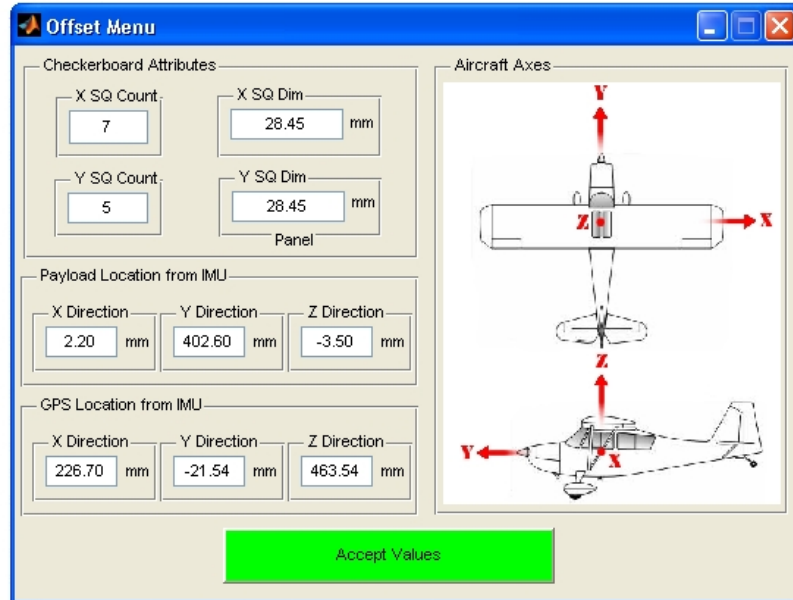


Figure 7-6. Offset menu in PolarisView for determining camera relative position and orientation

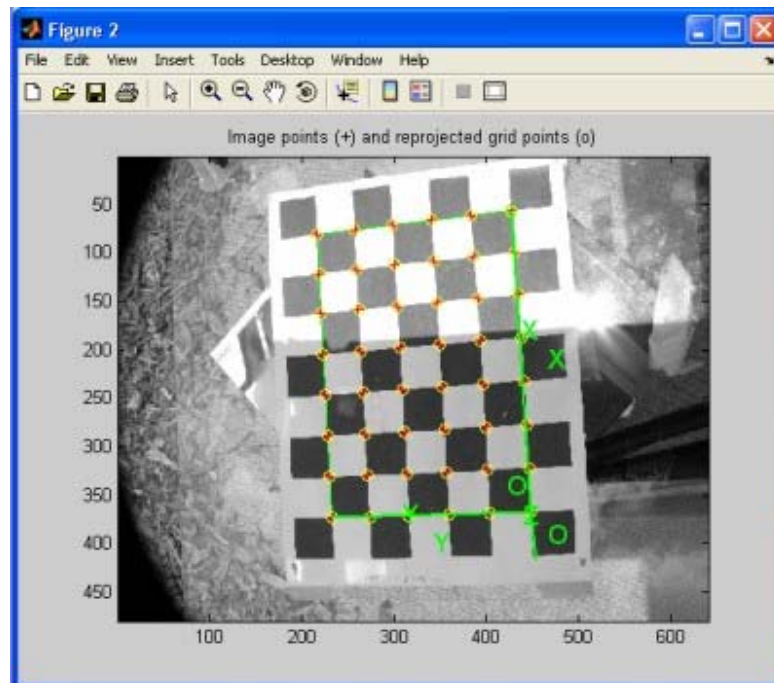


Figure 7-7. Example of calibration image of taken just before survey flight. Used for determining camera boresight misalignment in PolarisView.



Figure 7-8. Example of area coverage assessment generated from PolarisView. These yellow overlays represent estimated photographed area at time of exposure.

CHAPTER 8 MAPPING OUTPUT AND ANALYSIS

Data Set

A flight test was conducted to assess the spatial accuracies of the single photo direct georeferenced solution. Residual comparisons in object locations were accessed directly through geo-registered photos. This form of comparison simulates the real-world application of the Polaris UAV for rapid mapping missions and tests all elements of the georeferencing, and geo-registration processes. The compensated data set and target attributes used for analysis can be seen in Appendix A (Table A-1 – A-2).

The controlled surveying flight was conducted over an agricultural field with ample space to set out ground control points. Distinguishable numeric targets measuring 1.5 x 1.5 meters were placed in random locations all over the field (Figure 8-1). A WAAS enabled handheld GPS was used to take the coordinates of the center of the target and to ensure that the targets were placed at the same elevation on the landscape, eliminating any concerns regarding the test area's topography. Other distinguishable features in the photographs that were recognizable in Google Earth[®] were considered for comparison as well.

The flight plan resembled a figure-eight type pattern with elongated central legs for straight and level flight portions (Figure 8-2). The targets were scattered in the central region of the flight plan and were captured from various headings depending on the completion of the flight plan. Varying flying heights were conducted throughout the flight to investigate altitude effects in the georeferenced solution.

The survey flight was conducted for approximately 25 minutes in which time 234 photos were taken. A subset of 34 photos was used for comparison. Fifteen of the pictures either contained targets or road intersections that were selected for residual analysis. Multiple targets

were often identified in the same photograph as well as in different photographs, giving multiple estimates of the ground location of the same point at different attitudes.

Results

The goal of the testing conducted over the pre-surveyed area was to establish a direct georeferenced spatial accuracy metric as a beginning point for the UF program. All photos were registered in Google Earth® at their full resolution to enable numbers on the targets to be recognizable (Figure 8-3). The cursor in Google Earth was used to scroll over the target's center and the latitude/longitude position was recorded, establishing the residuals analyzed throughout (Figure 8-4).

Plots of the target's surveyed position versus the PolarisView mapped target position (Figure 8-5) is used as a graphical representation of the errors present in the georeferenced solution. The blue circle within the plots represents the surveyed target and the red 'x's' represent the locations recorded from Google Earth®. Multiple 'x's' are seen in some plots because multiple images identified the same target. A plot of the orientation of the UAV and camera at the time of commanded camera exposure (Figure 8-6) shows how tilted the UAV was while taking this set of pictures. A complete set of all target's spatial accuracies provide delta east (difference in East position), delta north (difference in North position), and a Euclidean distance measure which expresses the magnitude of the residuals which is the straight line distance between the actual and measured target (Figure 8-7). Root-mean-square errors of the Euclidean distances for all targets are compiled to compare accuracies (Figure 8-8).

At first glance, RMS errors in positional accuracies seem quite high, however, when the navigation suite, camera synchronization, and small aircraft technologies are considered, large sources of the error can be partially accounted for. It has been shown in literature that in low-dynamic, near-level flight conditions, the attitude solution is adequate, but is mentioned that in

larger banking and pitch situation the accuracy is compromised [30]. No in-situ flight data between the Kestrel IMU and a precision IMU exists so it is hard to quantify these inaccuracies.

In order to compare between RMS positional errors and aircraft orientation, a metric for the magnitude of average aircraft orientation per target was devised. This comparison shows a general trend that the larger the magnitude of roll and pitch, the larger the error in estimating a target's position (Figure 8-9). It is the author's opinion that this is derived from the degraded ability for the IMU to accurately measure larger attitude angles and not from the photogrammetric solution. A plot of theoretical IMU errors shows if both roll and pitch have an error of 1.5 degrees (not unlikely at higher attitude angles), Euclidean distance wise, the principal point could be as much as 15 meters off (Figure 8-10). Heading inaccuracies is a metric that was not isolated here, but should be considered. In [30] 1.1 degree error was realized. This can cause the most spatial inaccuracies where targets are located near the extents of the photo as they have a larger radius from the center of rotation.

One parameter of the direct georeferencing that is not completely accounted for is the camera sync error. Experimentally and through other source, it was determined that an 87 millisecond delay in camera exposure time exists. However, there is no way to properly synchronously link this offset timing to autopilot rate output. A plot of the UAV's pitch and roll rates during the first 20 photos illustrates the responsiveness of the radial and longitudinal axes (Figure 8-11). A plot of these rates integrated over 87 milliseconds at an altitude of 300 meters was shown to estimate part of the errors in the georeferenced solution (Figure 8-12). A contribution of approximately 15 meters of error could be present in the total solution from sync error alone.

The pre-surveying accuracies of the ground targets are only as accurate as the GPS they were recorded with. Due to inclement weather, the long process of using more sophisticated GPS equipment had to be bypassed. Consequently, a WAAS enabled hand-held GPS receiver was used and has at best a ± 3 meter accuracy. This could account for at least 3 meters of error. The current UAS GPS receiver is of standard accuracy, 15 meters (2d rms), however it has been shown that a trajectory projection of the “stepped” GPS samples can dramatically improve the solution. However, this is done in a post-processing environment where data has already been collected [30]. The current system uses real-time GPS data with extrapolated sub-second output, so it is unlikely that the autopilot is outputting this corrected GPS positioning which may result in an error of at least 3 meters.

Table 8-1. Indicates calculated boresight misalignments for the data set

Roll (Deg)	Pitch (Deg)	Yaw (Deg)
-2.4949	8.4322	3.2641

A

B



Figure 8-1. Examples of ground control targets used for spatial comparison in the mapping process. Targets are 1.5 meters square. A) Target 8 B) Target 17

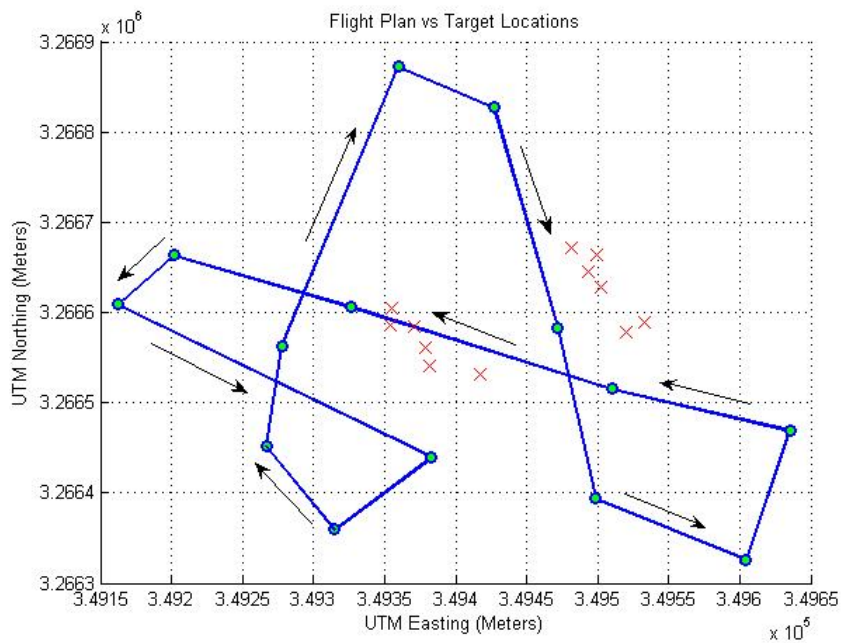


Figure 8-2. Polaris UAV flight route versus numeric target locations



Figure 8-3. Rectified images for data set are rectified and registered from PolarisView into Google Earth®'s interface

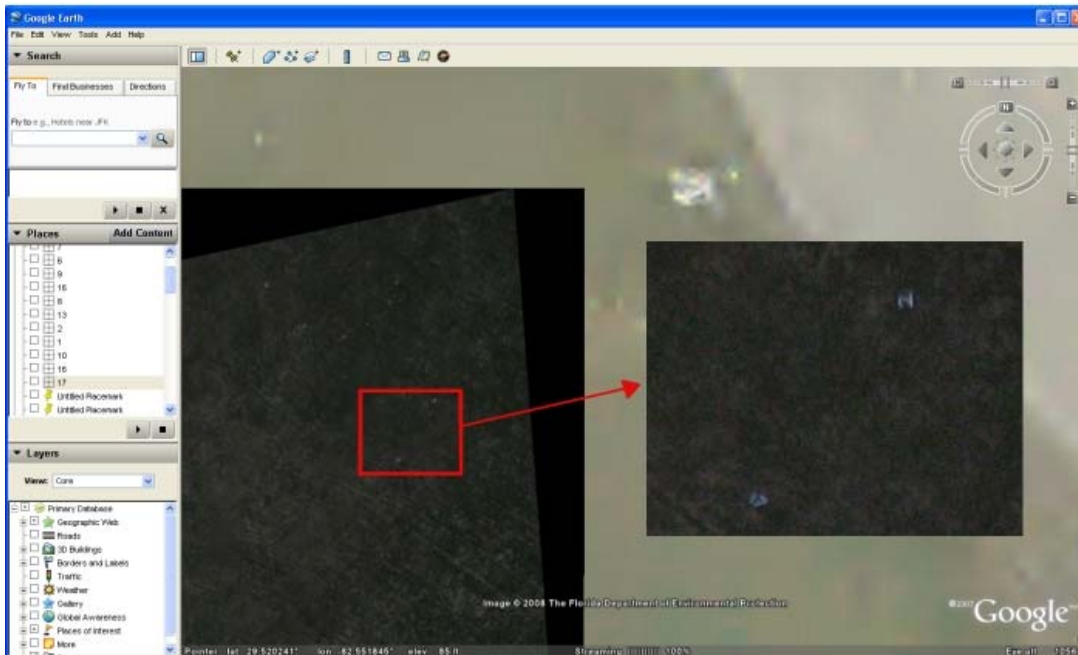
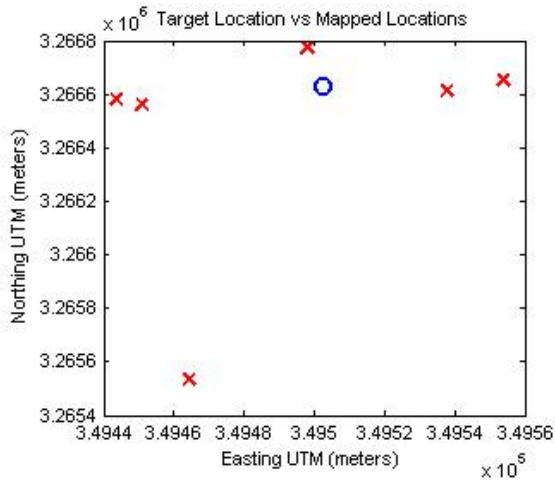
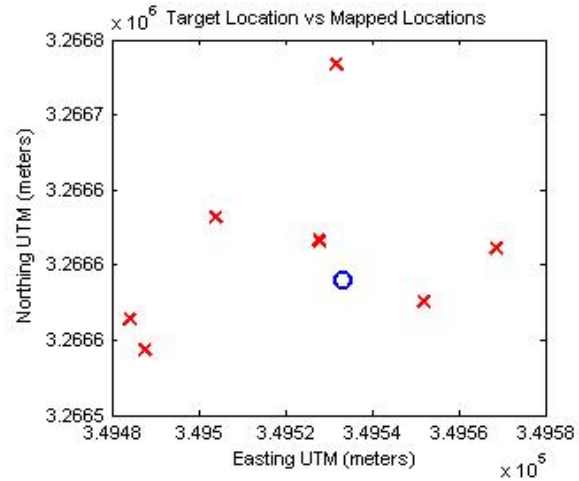


Figure 8-4. All pre-surveyed points were located in registered photos. The coordinates of the center of the target were used for comparison. Other photographs reveal man-made objects that are identifiable in the original map set. These are used for comparison as well.

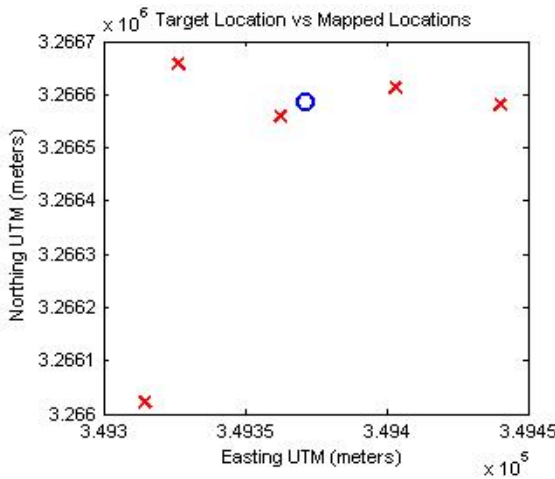
A



B



C



D

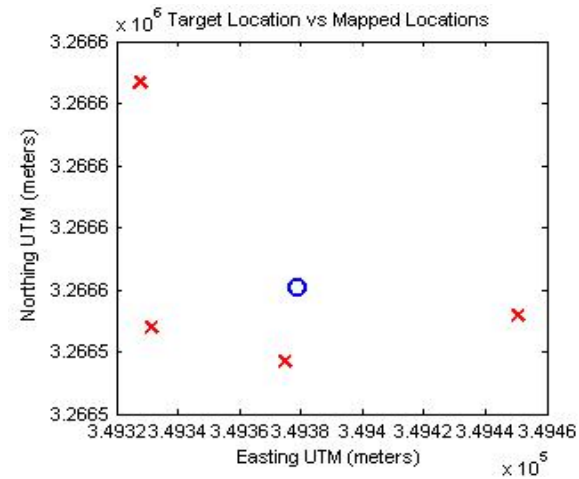


Figure 8-5. Plots A through N represent the pre-survey location of the target versus measured values for those targets through the photos in Google Earth . The ‘O’ represents the “actual” target and the ‘X’s” represent imaged coordinates. A) Target #1 B) Target #2 C) Target #5 D) Target #6 E) Target #7 F) Target #8 G) Target #9 H) Target #10 I) Target #11 J) Target #13 K) Target #16 L) Target #17 M) North street Intersection N) South Street Intersection

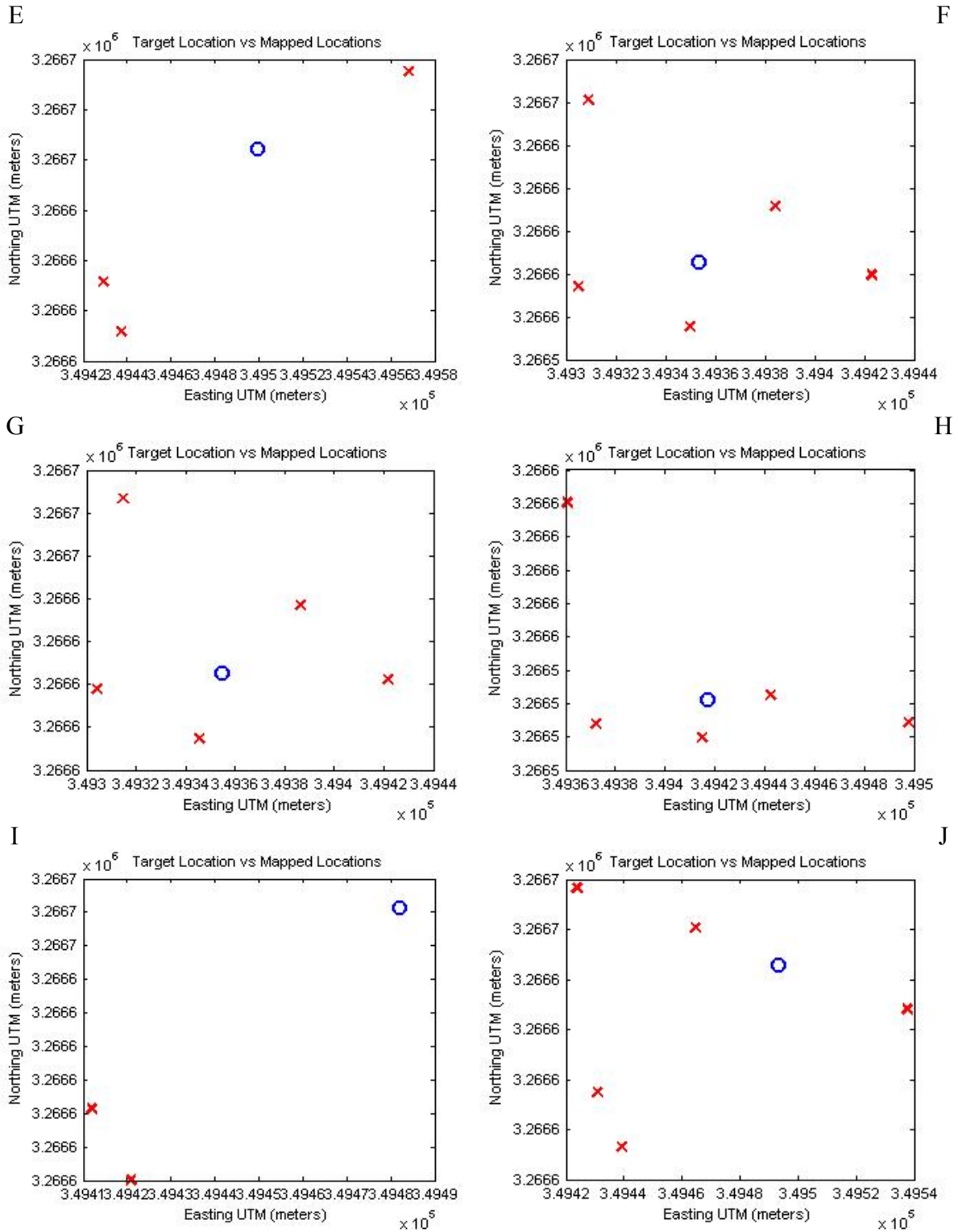
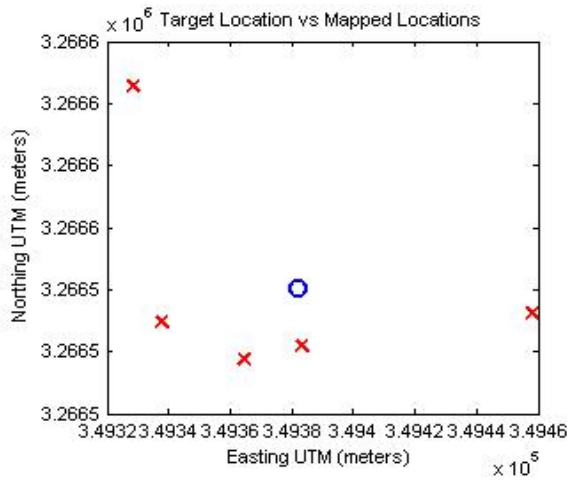
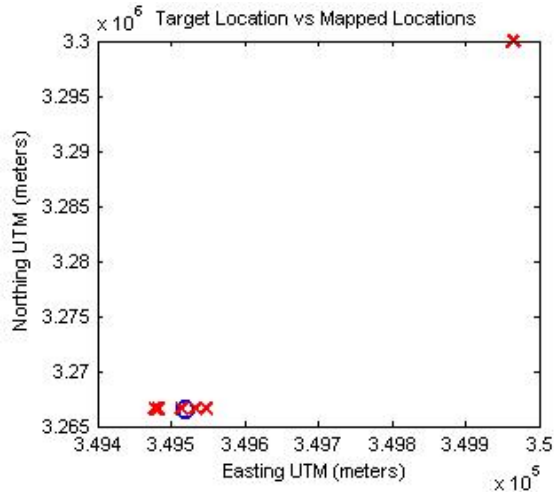


Figure 8-5. Continued

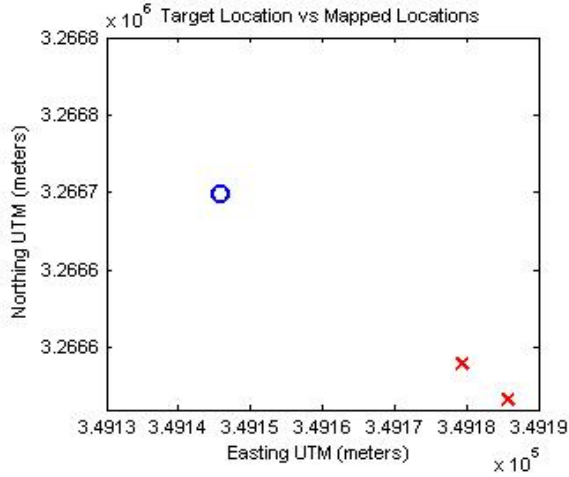
K



L



M



N

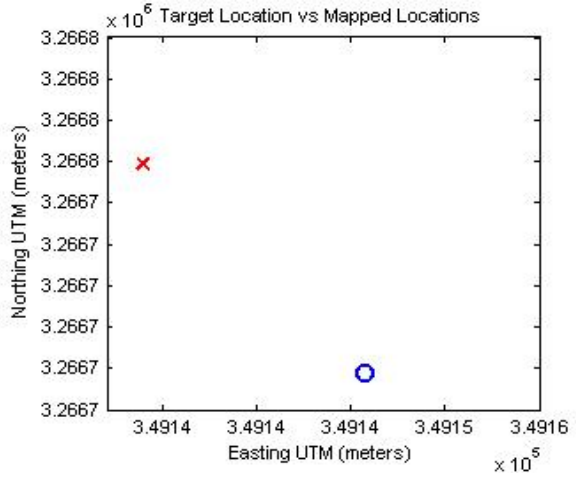


Figure 8-5. Continued

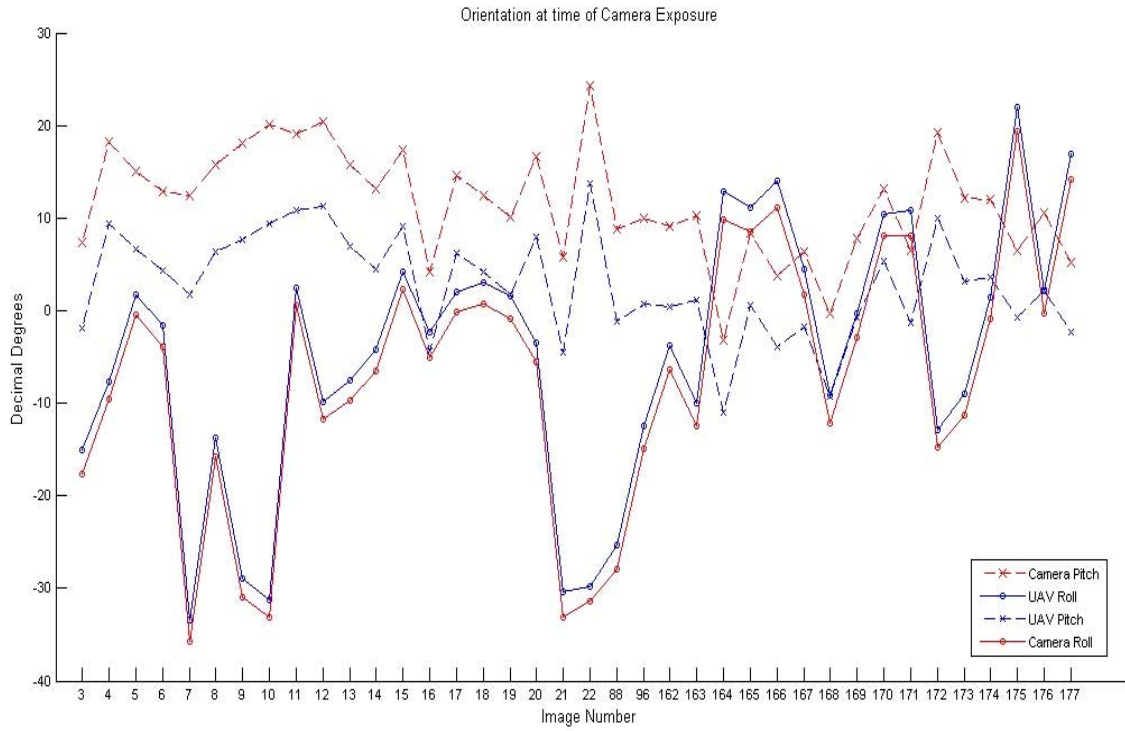


Figure 8-6. UAV and camera attitudes at the time of commanded camera exposure

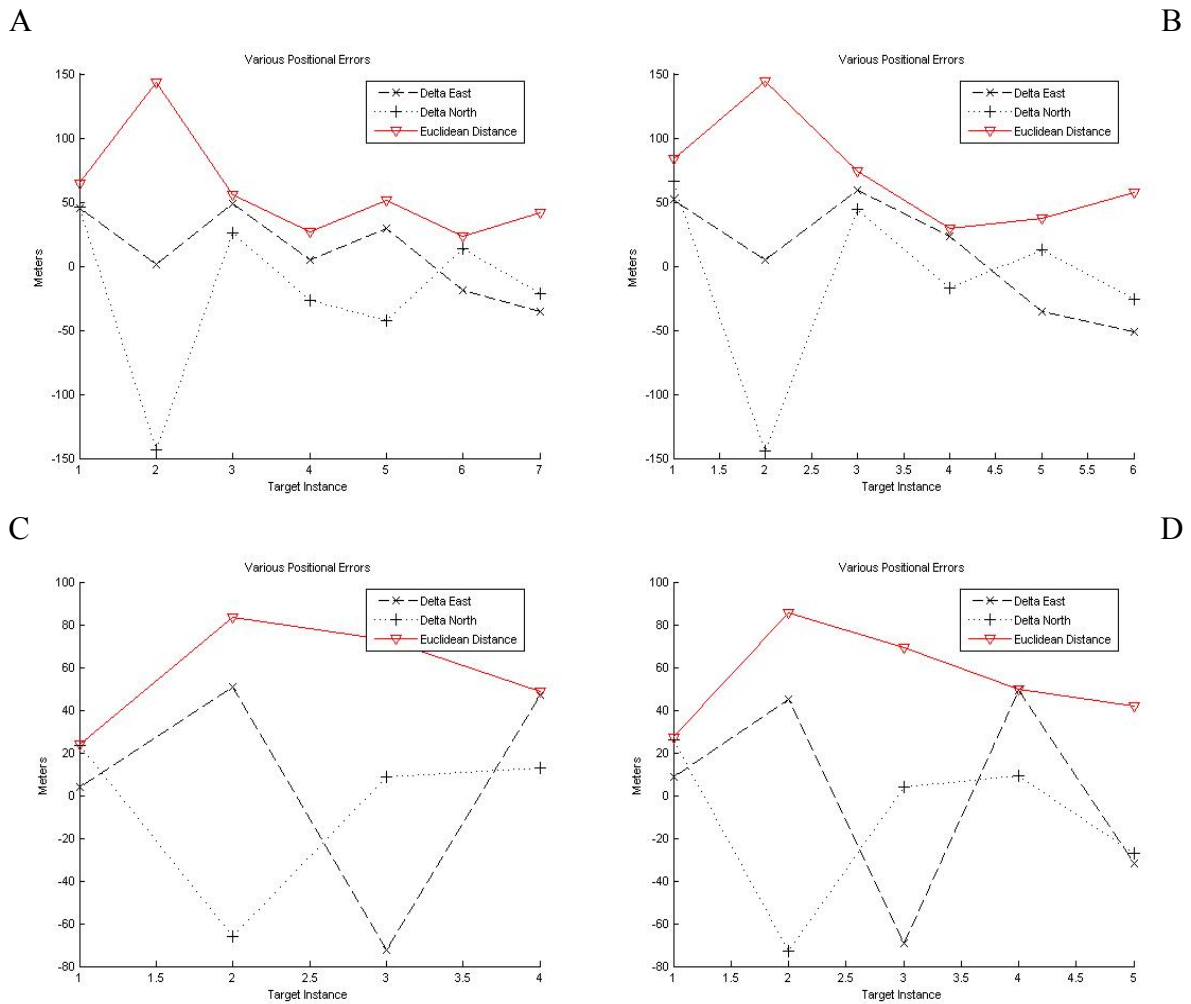
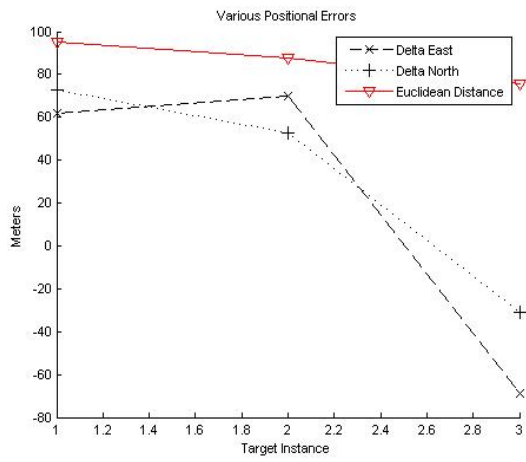
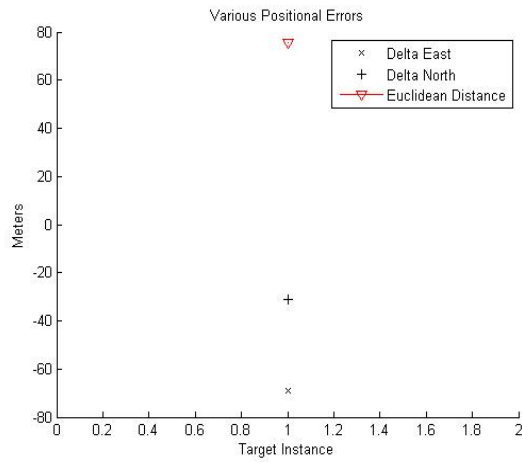


Figure 8-7. Plots A through N provide residuals for all registered photos. A) Target #1 B) Target #2 C) Target #5 D) Target #6 E) Target #7 F) Target #8 G) Target #9 H) Target #10 I) Target #11 J) Target #13 K) Target #16 L) Target #17 M) North street intersection N) South street Intersection

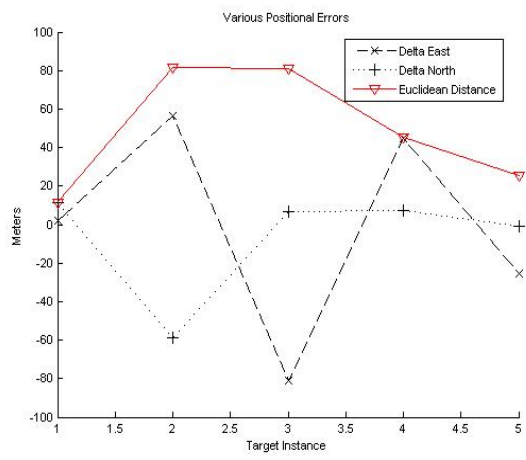
E



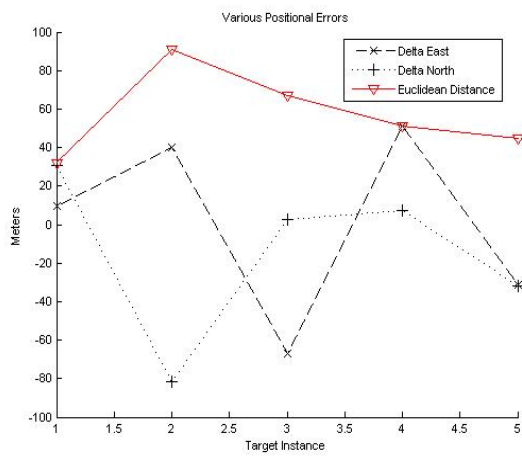
F



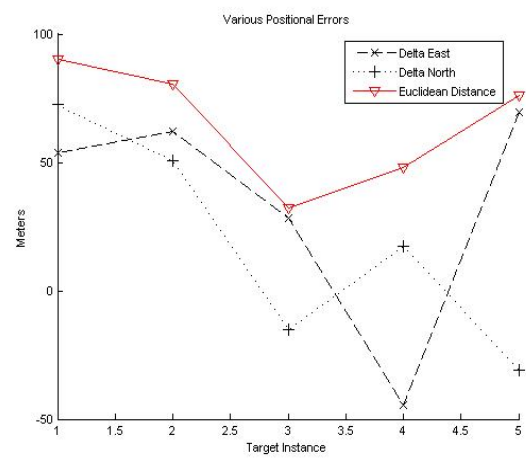
G



H



I



J

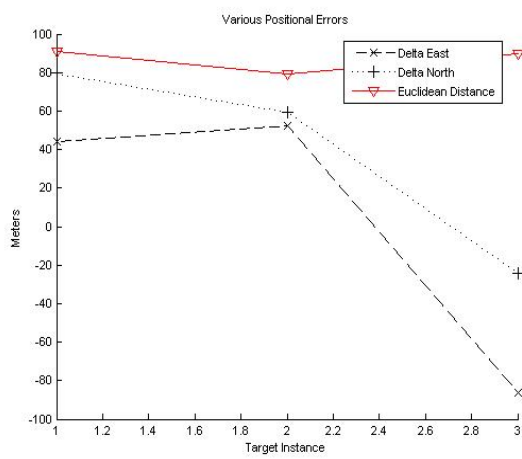
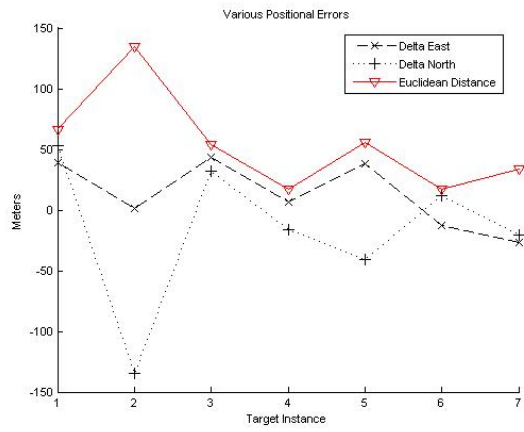
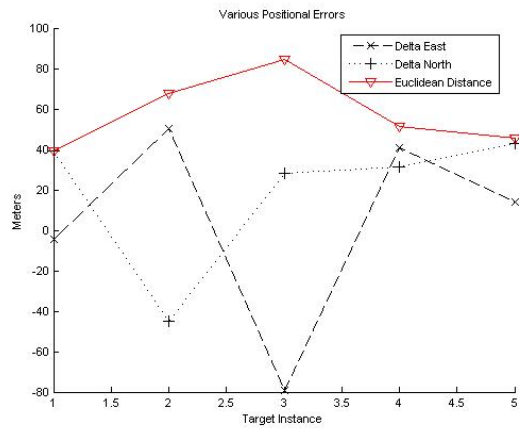


Figure 8-7. Continued

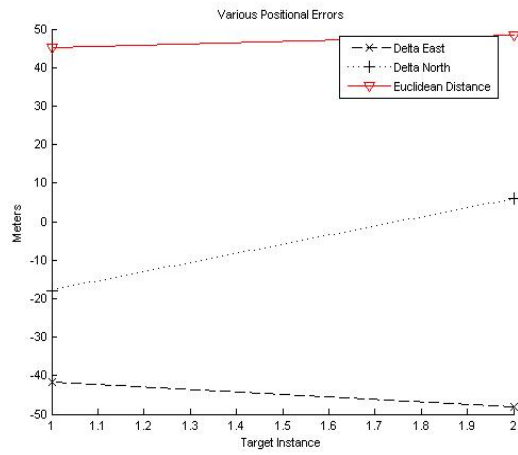
K



L



M



N

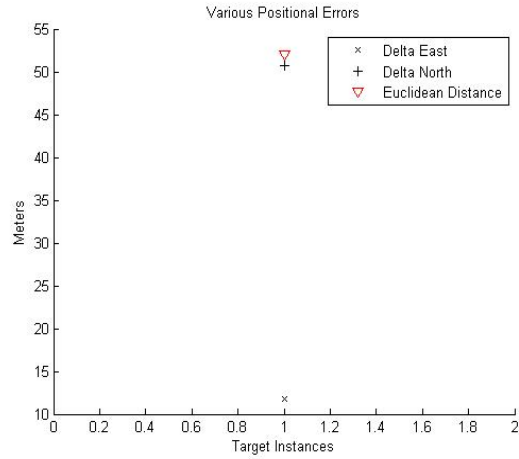


Figure 8-7. Continued

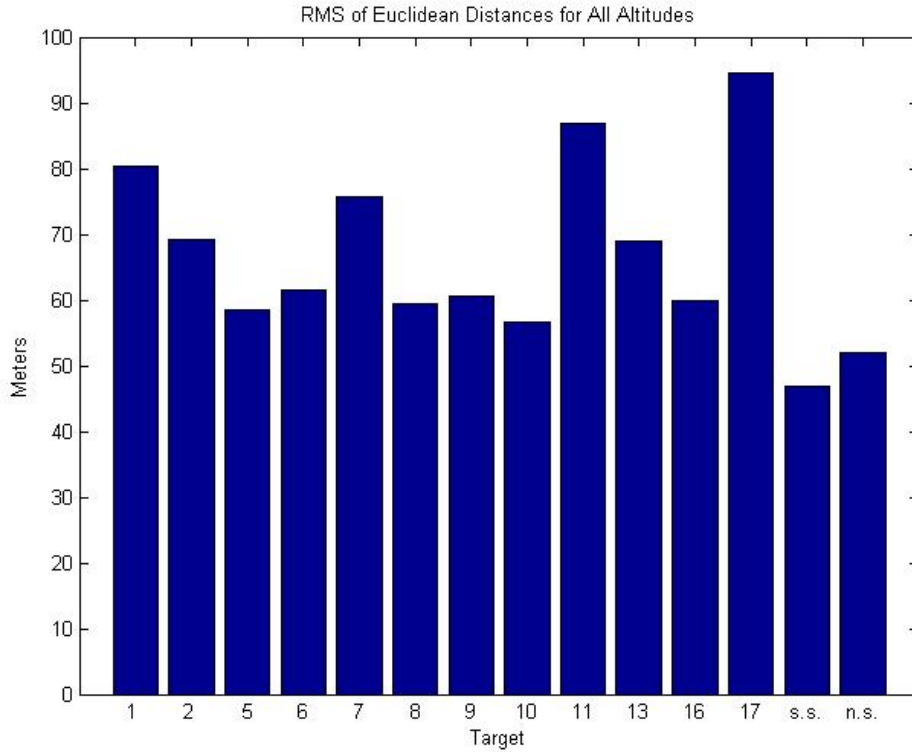


Figure 8-8. RMS of Euclidean distances for all targets. Ss and ns stand for south street intersection and north street intersection, respectively.

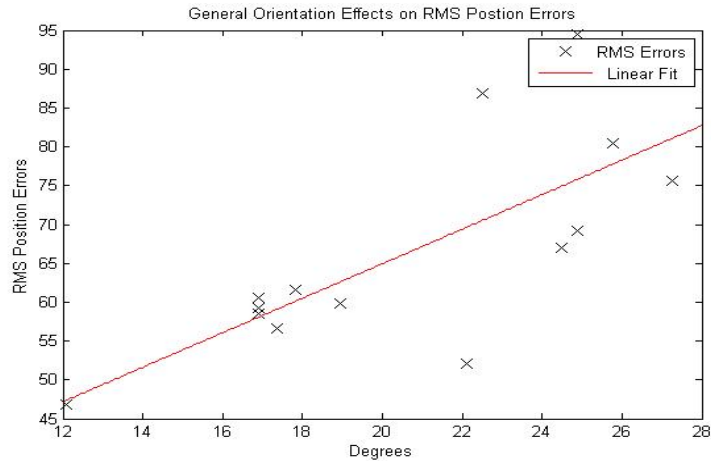


Figure 8-9. Averaged combined pitch and roll effects on positional accuracy apparent in data. A linear fit shows general tendencies.

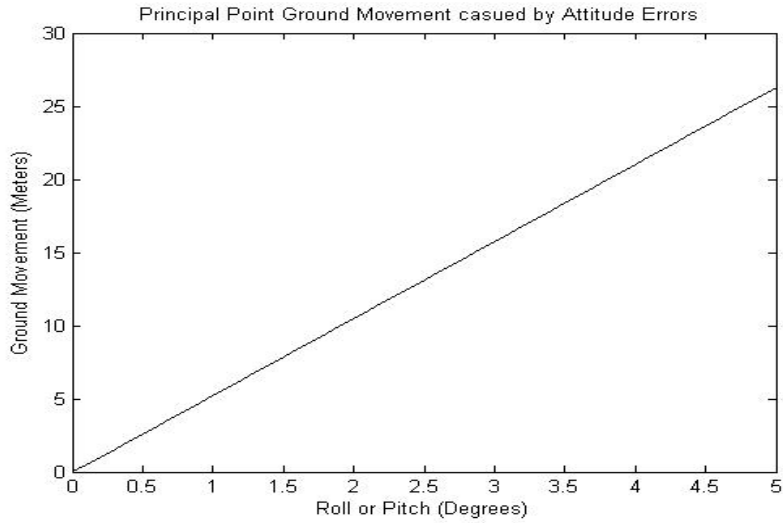


Figure 8-10. Simulated principal point error on the ground from IMU inaccuracies in pitch and roll.

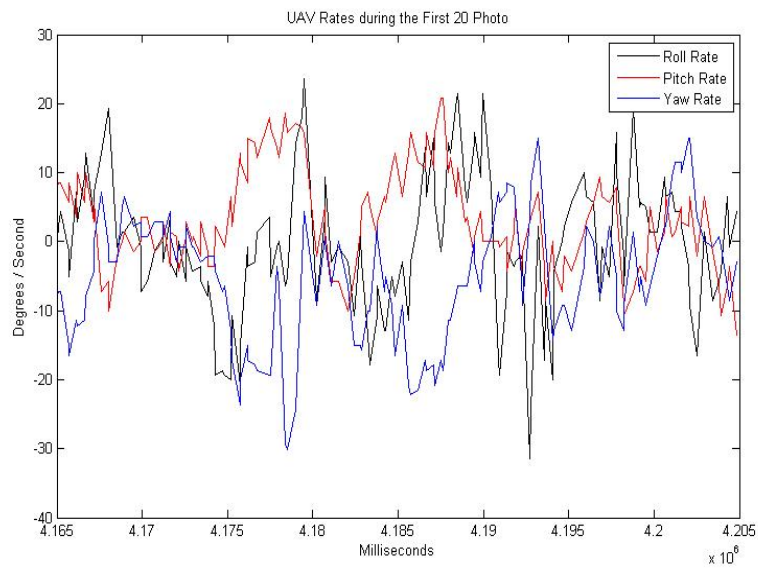


Figure 8-11. Rates of all UAV states during initial 20 photograph capture. Demonstrates the high dynamic nature of the UAV.

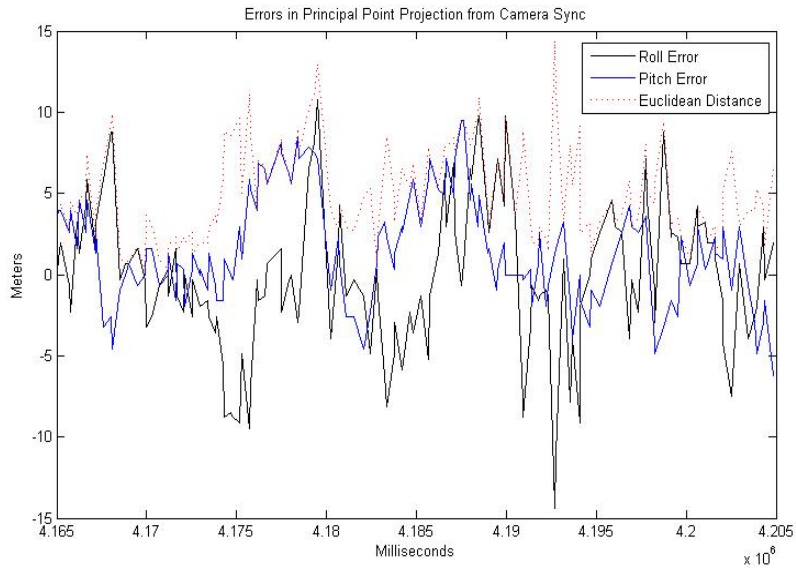


Figure 8-12. Unaccounted for effects of an 87 millisecond synchronization error with high dynamics present. This error represents errors in the principal point projection only from an altitude of 300 meters.

CHAPTER 9 SUMMARY, CONCLUSION AND RECOMMENDATIONS FOR FUTURE WORK

Summary

The purpose of this thesis was to assess the design and validity of the initial georeferenced output of the Polaris UAV. An array of customized electronic hardware and software was developed to allow the system to function as an autonomous direct georeferencing mapping platform. By comparing photographed target locations to that of their surveyed location, a measure of actual system performance was determined.

A test flight of varying altitudes was conducted in which 234 images were taken. An adequate amount of these photographs contained the 14 ground control targets. A subset of 34 images was selected to comprise a data set used for spatial analysis. A total of 62 instances of the control points were captured; 4.9% were identified within a 25 meter radius of their actual location, 36.5% within 50 meters, 27.6% within 75 meters, 21.3% within 100 meters, and 9.8% within 150 meters. Therefore, a 67.62 meter RMS error exists in the direct georeferenced image solution across all measurements. Since a benchmark was established, the results of the mapped images were considered a success.

Conclusion

It needs to be mentioned that the flight area that this test was conducted was constrictive due to a poor location of the ground operator relative to the flight area. The longer legs of the flight plan had to be shortened to keep the UAV in sight, making them much smaller than normal survey legs when a chase vehicle is often used. This path shortening didn't allow for the closed-loop control on the Polaris to settle adequately before initiating a new turn, resulting in few near-vertical pictures. Judging by the generalized relationship in camera attitude versus positional accuracy (Figure 8-9), these non-level flight conditions combined with non-level camera

mounting, resulted in larger error than what is potential for the system. Further, flight testing was conducted just before a fast moving frontal weather system which is known to have drastic ambient pressure differentials. This could have possibly caused the UAV to have erroneous barometric-based altitude readings; seriously affecting the georeferenced solution. Therefore, it is the author's opinion that the results found here are more than likely, a worse-case scenario.

Regardless of the error in positional accuracies, current technology can be very useful in large areas where non-distinguishable features exist and high spatial accuracy is not needed. For instance, the Lake Okeechobee levee-monitoring project that UF is involved in with the Corps of Engineers calls for rapid assessment of levee conditions before threatening weather, i.e. hurricanes, encroach. The goal is to be able to identify possible leaks in the levee with visible spectrum and thermal infrared imagery. The current technology of the Polaris (in the author's opinion) could satisfy these mission requirements. The Polaris could fly along the levee, capture georeferenced imagery with either imaging payload, and rapidly map those images so that civil engineers or an operations staff member could send repairmen to identified problem areas quickly, within a ~68 meter RMS radius. Current methods for leak detection involve driving on top of the levee for some 235 miles. With a range of approximately 15 miles, 16 flights could be performed to map the whole levee in a fraction of the time while producing organized data that can be used for many other purposes.

Recommendations for Future Work

Based on initial results, many improvements need to be considered to increase spatial accuracies in the mapped images. Improvements need to come from two main areas of focus which encompass many ideas for bettering the system. Majority of the improvements require hardware that may or may not be available and only future technology will dictate.

Georeferencing

Although the lightest platform is currently in use, an addition of a completely separate IMU and the implementation of a WAAS/DGPS GPS receiver with a PPS signal generator is the quickest way to improve the directly georeferenced solution. Though very feature rich in features for navigation and localization of video, the Procerus autopilot is a proprietary system and therefore restricts the abilities to alter data output. However, the current autopilot should remain as the navigation controller and means for subsystem message generation for the UAV. All things considered, the method developed in this thesis for synchronizing the camera to state data of the UAV is the best way.

However, if another IMU is used just for the payload, it should be mounted directly above the camera to eliminate the lever-arm offset and to isolate the boresight of the camera. In the opinion of the author, the IMU can remain MEMs-based (for weight) as long as an adequate sampling rate exists from the inertial sensors, so a trajectory solution can be generated in the post-processing steps using better developed state estimate techniques such as Kalman Filtering [39]. This will take longer, but can guarantee better accuracy. Similar to how PolarisView has the ability to adjust output resolution to save time, the method by which state estimates are generated could also be toggled in cases where speed over accuracy is required. The new WAAS GPS receiver can be shared amongst the autopilot and camera IMU and be synchronized by the PPS signal. A processor should remain in the loop to write all raw sensor data and PPS signal flag transmissions to the removable memory while simultaneously issuing a shutter on reception of the PPS. This will allow synchronized rate information to be provided before and aft the camera trigger flag so an integration of the rate data over the camera exposure time delay can take place rendering a better estimated orientation of the camera at the time of exposure.

A new camera should be selected for aerial mapping purposes. This camera does not necessarily have to be very expensive, but should have a larger image sensor and better optics than the current COTS camera. The camera should definitely have the ability to change features in real-time. A method of determining the exposure time delay has to be developed. This method should include some sort of in-situ feedback mechanism, rather than mathematical model, from the camera to the processor since the CCD array uses capacitive elemental excitation; discharge times between different photographed environments vary. Further, feedback from the camera's data storage to the processor needs to be implemented since the image file size is also dynamic based on the photographed environment. This causes variable camera buffer consumption and varying data card write times. The instance may exist where the camera is issued a shutter command but cannot physically store that picture, putting the system out of sync. Also, with a little more work the processor should continue to get attitude data from the autopilot so that it can determine when to take a photo based on aircraft attitude. This would solely be for reducing the amount of photos taken if storage is an issue. In general, for clarity and sharpness of the photos, it appears that higher relative groundspeeds due to rotational rates produce "fuzzier" images. Therefore, it is recommended that a camera have as high a shutter speed as possible and that the UAV be flown on a sunny day so a low f-stop setting can be used. On the other hand, minimizing the groundspeed would achieve the same effect. A supplemental control design implementation could achieve this.

The general procedures taken to directly georeference the images are not necessarily the cause of errors here. Due to the relatively flat relief found in Florida, only rectification of the photos is fine. However, other methods, namely orthorectification, exist to account for variable relief. In the case of the data set, orthorectification will improve the solution only minimally, but

in other mission areas this method may have to be used. In order to accomplish this practically, a more precise scanning-type altimeter where a swath of ground elevations can be determined, is needed. Until Lidar is miniaturized, some sort of range finder device could suffice. The stereo image method with aero triangulation exists, however, more photographs will have to be recorded in order to guarantee enough overlap, possibly causing digital storage issues.

Small Unmanned Aerial Vehicle Control

Two separate issues on “UAV control” should be considered for the next generation UAS. The first is very quickly obtainable and has been a long time coming and the other is a fresh idea based on results presented in this thesis.

In most situations, a “lawn mower” type survey pattern is desirable to cover all extents of a desired area. A software package needs to automatically generate a flight plan based on the defined outer-most bounds of a survey area. Currently, all intermediate waypoints for turns and transect spacing have to be added manually and is very time consuming. Virtual Cockpit provides a flexible method for adjusting these manual points and should still be taken advantage of; therefore, the future software should generate the waypoints as a .fpf (flight plan file) so Virtual Cockpit can import them. Parameters such as desired: transect width, radius of dog-bone turns, closed-loop settling time, airspeed, altitude, image overlap, and field of view should all be allowable inputs.

It is well known that small UAVs are susceptible to jerky, high dynamic behavior due to wind gust, thermals, etc. After realizing actual rates during synchronous imaging on the Polaris (Figure 8-11), recommendations can be made to minimize this effect. The Polaris currently uses an autopilot that has PID controllers for stability control of the aircraft. The controllers work well in most general cases, however, do not perform well when an external disturbance, i.e. wind, is introduced into the system. A robustifying term is needed in the control design in order

to “squash” or quickly minimize these disturbances. Often though, robust control requires a high energy cost for the actuators and doesn’t always respond well to cyclic input. An adaptive controller lacks the ability to squash the impulse nature of a disturbance but can account for unknowns in the plant model and disturbance. A Lyapunov-based control design called robust integral of the sign error (RISE) exists that exhibits the effects of both robust and adaptive control while still guaranteeing asymptotic stability [45]. Due to the slow framing rate of the hobby-type servos used in inexpensive small UAVs, this type of robust control may be required. In wind gust situations, it is the effect of cross-wind that contributes the most to undesired aircraft attitudes; therefore, it is recommended that a RISE-based controller be implemented on the roll axis and engaged during autonomous synchronized image segments. The idea is that the controller uses the additional camera’s IMU to dictate the roll rate performance of the aircraft, thereby optimizing the axial stability for direct georeferencing. The controller can be implemented on the subsystem control processor and have accessibility to the camera IMU’s high rate output and the servo output of the Procerus® autopilot. An adjustable weighted adder within the processor could inject more servo control based on the output of the RISE controller during high dynamic situations while still having the autopilot’s reliable navigation algorithms controlling majority of the flight control system.

APPENDIX A POLARISVIEW GENERATED DATASET

PolarisView provides more data than just the mapped output and a linked KML file. The software produces a tab delimited text file for the entire missions synch image data in a file called “Parsed_Pic_Data.txt”. This is automatically generated in the working directory selected by the user. Another file called “Compensated_Pic_Data.txt” is produced in the output directory (Figure A-1). This file displays compensated data based on boresight misalignment, lever-arm offsets and sync error estimates. Filtered values can be produced from the Compensated_Pic_Data by checking the filtered data box in the GUI and changing the tolerance values. The filtered data set is stored in a file called “Filtered_Pic_Data.txt” in the output directory.

All images overlaid in Google Earth® were inspected for targets and other ground control points. Upon discovery, the latitude and longitude coordinates were recorded for residual analysis. A table was devised with these coordinates and all other data pertaining to a particular target (Figure A-2).

Table A-1. Compensated_Pic_Data file used for rectification, area assessment and mapping in the results section

Pic #	Roll (Deg)	Pitch (Deg)	Heading (Deg)	Altitude (Meters)	Latitude (DecDeg)	Longitude (DecDeg)	Ground Track (Deg)	Airspeed (M/s)
3	-17.702057	7.348692	171.999131	302.650646	29.51843654	-82.55319974	156.646661	12.5
4	-9.591348	18.24883	141.069226	301.728292	29.51821166	-82.55298799	123.586996	13.15
5	-0.492459	15.027198	142.870648	301.043439	29.51804924	-82.55267542	127.712293	13.25
6	-3.955692	12.825514	148.9731	301.360062	29.51785994	-82.55241721	130.920856	12.9
7	-35.783686	12.467541	121.56131	299.175375	29.5176786	-82.55212351	106.856629	13.05
8	-15.835625	15.708724	21.875323	302.707527	29.51777679	-82.55139808	24.866368	12.9
9	-30.908914	18.050031	354.74449	299.211441	29.51847561	-82.5512511	1.375099	13.45
10	-33.137967	20.063285	290.522165	296.721063	29.51880934	-82.55138992	300.057997	13
11	0.509901	19.094982	274.281143	298.072045	29.51897826	-82.55175619	285.504869	12.6
12	-11.753432	20.355219	300.845786	299.407955	29.51923453	-82.55213669	309.626392	12.85
13	-9.6316	15.769382	274.593254	299.877959	29.51940177	-82.55248942	285.676757	13.5
14	-6.51899	13.153482	263.127387	302.361301	29.51949319	-82.5529238	273.873826	13.2
15	2.234168	17.322453	283.222693	299.727024	29.51960367	-82.55338227	293.698166	13.9
16	-5.079284	4.144479	276.759658	304.298989	29.5197227	-82.5537864	287.911292	13.5
17	-0.17745	14.548824	272.055169	299.706883	29.51982474	-82.5542062	282.23901	13.7
18	0.78446	12.426085	277.589629	300.692384	29.51991923	-82.55463294	288.140475	13.15
19	-0.844378	10.113675	282.245311	298.842248	29.51992009	-82.55500677	292.666842	13.25
20	-5.564566	16.54997	292.645785	298.551953	29.52024608	-82.55541048	302.521716	13.05
21	-33.111688	5.802998	252.182674	297.637701	29.52034568	-82.55575386	262.242783	13.45
22	-31.423657	24.358676	217.209649	296.914525	29.52016768	-82.55604625	220.244976	12.65
88	-27.893995	8.836426	355.93284	285.323833	29.51921026	-82.55378375	352.025269	13.8
96	-14.974885	9.912005	226.624425	230.668836	29.52025628	-82.55599473	228.724752	13.05
162	-6.357696	9.053145	57.548714	110.8328	29.51924313	-82.55333864	58.728174	11.65
163	-12.431692	10.220439	26.989725	107.505261	29.51943048	-82.55307627	29.621918	10.75
164	9.755034	-3.180418	112.179721	96.254604	29.51964905	-82.55235427	105.939896	10.1
165	8.527806	8.425522	145.008612	93.333823	29.5194665	-82.55197601	134.473195	9.5
166	11.196723	3.78087	189.570826	91.136202	29.51923797	-82.55184489	173.319733	9.4
167	1.757409	6.412629	223.474707	92.650568	29.51892043	-82.55188058	211.593314	10.5
168	-12.192761	-0.333726	233.709978	92.766558	29.5186737	-82.55207996	218.583399	10.2
169	-2.872878	7.760992	234.585145	89.325013	29.51843197	-82.55230827	218.125033	9.3
170	8.119902	13.180888	246.560649	85.033348	29.51822896	-82.55256897	231.761428	9.75
171	8.135832	6.568745	296.295096	87.820784	29.5181822	-82.55256982	290.661489	10.35
172	-14.757748	19.170419	295.86055	85.064699	29.51833325	-82.55314355	291.750109	12.1
173	-11.287602	12.117616	281.968584	90.68542	29.51874499	-82.5539836	275.535404	12.3
174	-0.904886	12.010828	275.334292	90.688861	29.51875532	-82.55428102	267.857769	12.05
175	19.378746	6.46507	291.440263	90.991452	29.51878082	-82.55460093	284.81732	12
176	-0.306252	10.48385	302.831246	84.178375	29.5189062	-82.55459942	300.000702	11.15
177	14.143055	5.200333	313.502077	85.313939	29.51912666	-82.5550863	311.746336	10.65

Table A-2. Pertinent data entries for a given target. This data was used throughout the thesis.

Target #	Latitude Estimate	Longitude Estimate	East UTM Estimate	North UTM Estimate	Delta East	Delta North	Euclidean Distance	RMS of Euclidean Dis	Roll of Cam	Pitch of Cam	Alti of Cam
1	29.5196	-82.5534	349450.8255	3266561.7946	51.7765	65.9237	83.8256	80.4227	0.5099	19.0950	298.0720
	29.5215	-82.5530	349498.0310	3266771.7617	4.5710	-144.0434	144.1159	80.4227	-11.7534	20.3552	299.4080
	29.5198	-82.5535	349443.4541	3266583.2854	59.1479	44.4329	73.9781	80.4227	-9.6316	15.7694	299.8780
	29.5204	-82.5531	349479.1755	3266644.7682	23.4265	-17.0499	28.9742	80.4227	-9.5913	18.2488	301.7283
	29.5201	-82.5525	349537.8204	3266615.2770	-35.2184	12.4412	37.3513	80.4227	9.7550	-3.1804	96.2546
	29.5205	-82.5524	349553.8452	3266653.7465	-51.2432	-26.0283	57.4746	80.4227	-27.8940	8.8364	285.3238
2	29.5195	-82.5530	349487.6178	3266543.7901	45.4975	45.8346	64.5820	69.2431	0.5099	19.0950	298.0720
	29.5212	-82.5526	349531.7395	3266733.4038	1.3759	-143.7790	143.7856	69.2431	-11.7534	20.3552	299.4080
	29.5196	-82.5531	349484.1012	3266563.5668	49.0142	26.0580	55.5104	69.2431	-9.6316	15.7694	299.8780
	29.5201	-82.5526	349527.9442	3266616.1848	5.1711	-26.5600	27.0587	69.2431	-9.5913	18.2488	302.3613
	29.5202	-82.5529	349503.9168	3266631.8018	29.1985	-42.1770	51.2977	69.2431	2.2342	17.3225	299.7270
	29.5197	-82.5524	349552.0294	3266575.8496	-18.9141	13.7752	23.3987	69.2431	9.7550	-3.1804	96.2546
	29.5201	-82.5522	349568.5943	3266611.2083	-35.4790	-21.5836	41.5284	69.2431	-27.8940	8.8364	285.3238
5	29.5196	-82.5543	349362.4759	3266559.3177	8.6824	25.8207	27.2414	58.4514	-9.5913	18.2488	302.3613
	29.5205	-82.5547	349326.3750	3266658.0056	44.7833	-72.8672	85.5287	58.4514	2.2342	17.3225	299.7270
	29.5198	-82.5535	349440.1275	3266581.0022	-68.9691	4.1362	69.0931	58.4514	-5.0793	4.1445	304.2990
	29.5197	-82.5547	349322.0797	3266576.0406	49.0786	9.0978	49.9147	58.4514	-0.1774	14.5488	299.7069
	29.5201	-82.5539	349403.2208	3266612.1984	-32.0625	-27.0600	41.9553	58.4514	0.7845	12.4261	300.6924
6	29.5194	-82.5542	349374.6832	3266536.9863	3.9034	23.6678	23.9875	61.6016	-9.5913	18.2488	302.3613
	29.5202	-82.5547	349327.7003	3266626.6198	50.8863	-65.9657	83.3120	61.6016	2.2342	17.3225	299.7270
	29.5195	-82.5534	349450.6937	3266551.9315	-72.1072	8.7226	72.6328	61.6016	-5.0793	4.1445	304.2990
	29.5195	-82.5546	349331.3990	3266547.9841	47.1876	12.6700	48.8590	61.6016	-0.1774	14.5488	299.7069
7	29.5199	-82.5536	349437.5557	3266591.6773	61.6578	72.6637	95.2980	52.9778	0.5099	19.0950	298.0720
	29.5201	-82.5536	349429.2927	3266611.7391	69.9208	52.6019	87.4979	52.9778	-9.6316	15.7694	299.8780
	29.5208	-82.5522	349568.1666	3266695.3423	-68.9531	-31.0013	75.6017	52.9778	-27.8940	8.8364	285.3238
8	29.5195	-82.5545	349349.9204	3266555.6061	3.7911	29.7655	30.0060	59.3118	-9.5913	18.2488	302.3613
	29.5205	-82.5549	349309.0652	3266661.2298	44.6462	-75.8581	88.0212	59.3118	2.2342	17.3225	299.7270
	29.5198	-82.5537	349423.0461	3266579.5678	-69.3346	5.8038	69.5771	59.3118	-5.0793	4.1445	304.2990
	29.5197	-82.5549	349305.0893	3266574.1619	48.6222	11.2098	49.8976	59.3118	-0.1774	14.5488	299.7069
	29.5201	-82.5541	349384.0189	3266611.6791	-30.3075	-26.3075	40.1326	59.3118	0.7845	12.4261	300.6924

Table A-2. Continued

9	29.5197	-82.5545	349345.5227	3266574.7296	9.4247	30.5769	31.9965	60.6211	-9.5913	18.2488	302.3613
	29.5207	-82.5548	349314.6416	3266686.7595	40.3058	-81.4529	90.8798	60.6211	2.2342	17.3225	299.7270
	29.5200	-82.5537	349421.7034	3266602.4190	-66.7560	2.8875	66.8184	60.6211	-5.0793	4.1445	304.2990
	29.5199	-82.5549	349304.0510	3266598.0066	50.8964	7.2999	51.4173	60.6211	-0.1774	14.5488	299.7069
	29.5203	-82.5541	349386.1998	3266637.0326	-31.2524	-31.7261	44.5338	60.6211	0.7845	12.4261	300.6924
10	29.5192	-82.5538	349414.9782	3266519.9324	1.9942	11.3900	11.5632	56.6792	-9.5913	18.2488	302.3613
	29.5199	-82.5543	349360.6599	3266590.2666	56.3124	-58.9443	81.5201	56.6792	2.2342	17.3225	299.7270
	29.5193	-82.5529	349497.8284	3266524.3674	-80.8560	6.9549	81.1546	56.6792	-5.0793	4.1445	304.2990
	29.5193	-82.5542	349372.2805	3266524.0500	44.6919	7.2723	45.2797	56.6792	-0.1774	14.5488	299.7069
	29.5193	-82.5535	349442.3866	3266532.4236	-25.4143	-1.1013	25.4381	56.6792	-6.3577	9.0531	110.8328
11	29.5199	-82.5537	349420.9575	3266590.1256	60.8981	81.0977	101.4171	51.7379	0.5099	19.0950	298.0720
	29.5201	-82.5538	349412.0323	3266611.4155	69.8233	59.8078	91.9362	51.7379	-9.6316	15.7694	299.8780
13	29.5197	-82.5535	349439.2469	3266573.1442	53.8993	72.4349	90.2881	66.9809	0.5099	19.0950	298.0720
	29.5199	-82.5536	349431.0046	3266594.7575	62.1416	50.8216	80.2771	66.9809	-9.6316	15.7694	299.8780
	29.5205	-82.5533	349464.6514	3266660.5908	28.4948	-15.0117	32.2072	66.9809	-9.5913	18.2488	302.3613
	29.5202	-82.5525	349537.7013	3266628.1362	-44.5551	17.4429	47.8478	66.9809	9.7550	-3.1804	96.2546
	29.5206	-82.5524	349553.5463	3266674.9211	-60.4000	-29.3420	67.1500	66.9809	-27.8940	8.8364	285.3238
16	29.5192	-82.5541	349383.3006	3266521.6859	-4.7141	38.9682	39.2523	59.7989	-9.5913	18.2488	302.3613
	29.5200	-82.5547	349328.5863	3266605.8807	50.0003	-45.2266	67.4202	59.7989	2.2342	17.3225	299.7270
	29.5193	-82.5533	349457.9964	3266532.5476	-79.4099	28.1065	84.2372	59.7989	-5.0793	4.1445	304.2990
	29.5193	-82.5546	349337.8395	3266529.3875	40.7471	31.2666	51.3607	59.7989	-0.1774	14.5488	299.7069
	29.5192	-82.5543	349364.5343	3266517.5031	14.0522	43.1510	45.3814	59.7989	-11.2876	12.1176	90.6854
17	29.5193	-82.5531	349481.0555	3266524.2590	18.1580	140.0820	141.2540	94.4614	0.5099	19.0950	298.0720
	29.5210	-82.5527	349518.6640	3266712.5187	-19.4506	-48.1777	51.9559	94.4614	-11.7534	20.3552	299.4080
	29.5195	-82.5531	349477.2644	3266545.2585	21.9491	119.0825	121.0884	94.4614	-9.6316	15.7694	299.8780
	29.5199	-82.5528	349514.0755	3266593.9802	-14.8620	70.3608	71.9133	94.4614	-9.5913	18.2488	302.3613
	29.5201	-82.5531	349482.5048	3266618.2327	16.7086	46.1083	49.0424	94.4614	2.2342	17.3225	299.7270
	29.5197	-82.5526	349532.7912	3266565.3549	-33.5778	98.9861	104.5261	94.4614	9.7550	-3.1804	96.2546
	29.5200	-82.5524	349546.9974	3266598.3067	-47.7839	66.0343	81.5097	94.4614	-27.8940	8.8364	285.3238
s_street	29.5198	-82.5562	349179.4676	3266590.0305	-41.6342	-17.8422	45.2963	46.8666	0.7845	12.4261	300.6924
	29.5196	-82.5561	349185.8366	3266566.1144	-48.0033	6.0739	48.3860	46.8666	-0.8444	10.1137	230.6688
n_street	29.5213	-82.5567	349133.9060	3266749.4758	11.8268	-50.7019	52.0630	52.0630	-5.5646	16.5500	298.5519

APPENDIX B
DEVICE PARAMETERS

Table B-1. Autopilot Sensor Parameters

Sensor	Description	Value
Rate Gyros	Dynamic Range	9° / sec
	Frequency Response	14 Hz
	Resonant Frequency	0.0318 kHz
	Resolution	0.1° / LSB
	Noise Density	22° / sec / \sqrt{Hz}
	Bandwidth	9 Hz
Accelerometers	Dynamic Range	10 g's
	Frequency Response	0.00150 Hz
	Resonant Frequency	200 kHz
	Resolution	±300 g / LSB
	Noise Density	±10 $\mu g\sqrt{Hz}$ rms
Barometric Pressure - Altitude	Resolution	0.249 meters

Table B-2. Canon A650 IS Parameters

Description	Value
Sensor Type	CCD
Effective Pixels	12.1 Megapixels
Image Resolution	4000 x 3000 pixels
Sensor Size Format	1/1.7
Sensor Physical Size	7.60 mm x 5.70 mm
Pixel Size	1.90 μm
Pixel Ground Coverage @ 100 m	23.57 mm
Viewing Angle	50.48° x 39.17°
Image Compression	Motion JPEG
Movie Compression	AVI
Focal Length	7.4 – 44.4 mm
Maximum Aperture	f/2.8 (W) – f/4.8 (T)
Shutter Speed	15-1/2000 sec.
ISO Sensitivity	80/100/200/400/800/1600
Exposure Compensation	± 2 stops in 1/3-stop increments
White Balance	Auto, Custom

LIST OF REFERENCES

- [1] Paine, D.P., Kiser, J.D., *Aerial Photography and Image Interpretation, Second Edition*, John Wiley and Sons, Inc., Hoboken, New Jersey, 2003.
- [2] Sasse, D. B., “Job-Related Mortality of Wildlife Workers in the United States, 1937-2000,” *Wildlife Society Bulletin*, Vol. 31, No. 4 (Winter, 2003), pp. 1015-1020.
- [3] Winslow, Megan V., 2008. “Four victims identified in plane crash in western Martin County,” *TCPalm*, March 13th.
- [4] Jones, P., “The Feasibility of Using Small Unmanned Aerial Vehicles for Wildlife Research,” MS Thesis, The University of Florida, 2003.
- [5] Lee, K., “Development of Unmanned Aerial Vehicle (UAV) for Wildlife Surveillance,” MS Thesis, The University of Florida, 2004.
- [6] Abd-Elrahman, A., Pearlstine, L., Percival, F., “Development of Pattern Recognition Algorithm for Automatic Bird Detection from Unmanned Aerial Vehicle Imagery,” MS Thesis, The University of Florida, 2004.
- [7] Wilkinson, B., “The Design of Georeferencing Techniques for Unmanned Autonomous Aerial Vehicle Video for use with Wildlife Inventory Surveys: A Case Study of the National Bison Range, Montana,” MS Thesis, The University of Florida, 2007.
- [8] J.-Y. Bouguet. *Camera Calibration Toolbox for Matlab*. http://www.vision.caltech.edu/bouguetj/calib_doc/index.html, 2001.
- [9] Federal Aviation Administration: Unmanned Aircraft Operations in the National Airspace System. Docket No. FAA-2006-25714. Federal Aviation Administration, Washington, DC (2007).
- [10] United States Government Accountability Office: Unmanned Aircraft Systems, “Federal Actions Needed to Ensure Safety and Expand Their Potential Uses within the National Airspace System,” Docket No. GAO-08-511. Government Accountability Office, Washington, DC (2008).
- [11] Morris, Stephen J., *Miniature Spy Planes: The Next Generation of Flying Robot*, Frontiers of Engineering, National Academy Press Washington, DC, 2002.
- [12] Grasmeyer, J., Keenon, M., “Development of the Black Widow Micro Air Vehicle,” AIAA Paper No. 2001-0127, January 2001.
- [13] Albertani, R., Hubner, P., Ifju, P., Lind, R., “Wind Tunnel Testing of Micro Air Vehicles at Low Reynolds Numbers,” SAE World Conference, SAE Paper No. 2004-01-3090, November 2004.

- [14] Claxton, D., Johnson, B., Stanford, B., Sytsma, M., “Development of a Composite Bendable-Wing Micro Air Vehicle,” 10th Annual International Micro Air Vehicle Competition, Brigham Young University, Provo, Utah, May 2006.
- [15] Albertani, R., Boria, F., Bowman, S., Claxton, D., Crespo, A., Francis, C., Ifju, P., Johnson, B., Lee, K., Morton, M., Sytsma, M., “Development of Reliable and Mission Capable Micro Air Vehicles,” 9th Annual International Micro Air Vehicle Competition, Konkuk University, Seoul, South Korea, May 2005.
- [16] Pounds, LaTrea (2006) “ARA’s Nighthawk: Battlefield in the Palm of your Hand”, Unmanned Systems, March 2006, Pg 40.
- [17] Watts, Adam, Bowman, W., Abd-Elrahman, A, Mohamed, A, Perry, J, Kaddoura, Y, and Lee, K (March 2008), “Unmanned Aircraft Systems (UASs) for ecological research and natural-resource monitoring”, *Journal of Ecological Restoration*, Vol. 26, No. 1.
- [18] Tian, L., Xiang, H., “Autonomous Aerial Image Georeferencing for an UAV-Based Data Collection Platform Using Integrated Navigation System,” 2007 ASABE Annual International Meeting, Minneapolis, Minnesota, ASABE Paper 073046.
- [19] Zhou1, G., Li, C., Cheng, P., “Unmanned Aerial Vehicle (UAV) Real-time Video Registration for Forest Fire Monitoring,” *Proceedings of IEEE International Conference on Geoscience and Remote Sensing Symposium*, Volume 4, 2005, pp 1803-1806.
- [20] Johnson, L.F., Herwitz, S., Dunagan, S., Lobitz, B., Sullivan, D., Slye, R., “Collection of Ultra High Spatial and Spectral Resolution Image Data over California Vineyards with a Small UAV,” *Proceedings, Int’l Symposium on Remote Sensing of Environment*, 2003.
- [21] Simpson, A., Stombaugh, T., Wells, L., Jacob, J., “Imaging Techniques and Applications for UAV’s in Agriculture,” 2003 ASAE Annual International Meeting, Las Vegas, Nevada, ASAE Paper 031105.
- [22] Herwitz, S.R., Johnson, L.F., Dunagand, S.E., Higgins, R.G., Sullivan, D.V., Zheng, J., Lobitz, B.M., Leung, J.G., Gallmeyer, B.A., Aoyagi, M., Slye, R.E., Brass, J.A., “Imaging from an unmanned aerial vehicle: agricultural surveillance and decision support,” *Computers and Electronics in Agriculture*, Volume 44, (2004), pp. 49–61.
- [23] Pearlstine, L., Percival, F., Carthy, R., Abd-Elrahman, A., Morris, S. (2001). Development of a Practical Unmanned Aerial Vehicle for Natural Resource Sampling. *Proceedings of the 18th Biennial ASPRS Workshop on Color Photography & Videography in Resource Assessment*.
- [24] Caltabiano, D., Muscato, G., Orlando, A., Federico, C., Giudice, G., Guerrieri, S., “Architecture of a UAV for volcanic gas sampling,” *Proceedings of IEEE International Conference on Emerging Technologies and Factory Automation*, Volume 1, 2005, pp. 739-744.

- [25] NOAA (No Author Listed). *NOAA and Partners Conduct First Successful Unmanned Aircraft Hurricane Observation by Flying Through Ophelia*.
<http://www.noaanews.noaa.gov/stories2005/s2508.htm>
- [26] Legat, K., “Approximate Direct Georeferencing in National Coordinates,” *ISPRS Journal of Photogrammetry & Remote Sensing*, Volume 60, (2006), pp. 239–255.
- [27] Ladd, G., Nagchaudhuri, A., Earl, T., Mitra, M., Bland, G. “Rectification, Georeferencing, and Mosaicking of Images Acquired with Remotely Operated Aerial Platforms,” ASPRS 2006 Annual Conference, Reno, Nevada, May 2006.
- [28] Kumar, P., Singh, V., Reddy, D., “Advanced Traveler Information System for Hyderabad City,” *Proceedings of IEEE International Conference on Intelligent Transportation Systems*, Volume 6, 2005, pp. 26-37.
- [29] Hruska, R., Lancaster, G., Harbour, J., Cherry, S., “Small UAV-Acquired, High-Resolution, Georeferenced Still Imagery,” Wildlife Society 12th Annual Conference, September 2005.
- [30] Perry, J., Mohamed, A., Abd-Elrahman, A., Bowman, S., Kaddoura, Y., Watts, A., “Precision Directly Georeferenced Unmanned Aerial Remote Sensing System: Performance Evaluation,” *Conference Proceedings for ION NTM*, 2008.
- [31] Mohamed, Ahmed, Rob Price (2002) “Near the Speed of Flight, Aerial mapping with GPS/INS Direct Geo-referencing”, GPS World magazine, March 2002, Vol. 13, No 3.
- [32] Weng, J., Cohen, P., Herniou M., “Camera Calibration with Distortion Models and Accuracy Evaluation,” *Proceedings of IEEE International Conference on Pattern Analysis and Machine Intelligence*, Volume 14, 1992, pp. 965-980.
- [33] Heikkilä, J., Silvén, O., “A Four-step Camera Calibration Procedure with Implicit Image Correction,” *Proceedings of IEEE International Conference on Computer Vision and Pattern Recognition*, Volume 17, 1997, pp. 1106-1112.
- [34] Burnside, C.D., *Mapping from Aerial Photographs, Second Edition*, Halsted Press a division of John Wiley and Sons, Inc., New York, New York, 1985.
- [35] Hemmleb, M., Wiedemann, A., “Digital Rectification and Generation of Orthoimages in Architectural Photogrammetry,” CIPA International Symposium, Göteborg, Sweden, Volume 32, 1997, pp.261-267.
- [36] Procerus Technologies, “Kestrel User Guide Kestrel Autopilot (firmware version MA8) & Virtual Cockpit 2.3,” Version 1.51, www.procerusuav.com, 2006.

- [37] ATmega128, ATmega128L Summary. Atmel Corporation. (2007), Rev. 2467P–AVR–08/07.
- [38] ATmega8, ATmega8L Summary. Atmel Corporation. (2007), Rev. 2486S–AVR–08/07.
- [39] Schwarz, K.P and M. Wei (2000), INS/GPS integration for Geodetic Applications, Lecture Notes for ENGO 623, Department of Geomatics Engineering, The University of Calgary, Canada.
- [40] *Conversion of Geodetic coordinates to the Local Tangent Plane*, Portland State Aerospace Society, Version 2.01 (2007).
- [41] Klein, V., Morelli, E., *Aircraft System Identification, Theory and Practice*, The American Institute of Aeronautics and Astronautics, Inc., Reston, Virginia, 2006.
- [42] Ressler, C., The Impact of Conformal Map Projections on Direct Georeferencing, *International Archives of the Photogrammetry, Remote Sensing and Spatial Information Sciences*, 34 (2002) (Part 3A), pp.283-288.
- [43] Crane, C., Duffy, J., *Kinematic Analysis of Robot Manipulators*, Cambridge University Press, 1998.
- [44] Wolf, P.R., and Dewitt, B.A., 2000. *Elements of Photogrammetry with Applications in GIS*, McGraw-Hill Science/Engineering/Math, New York, N.Y.
- [45] P. M. Patre, W. Mackunis, C. Makkar, and W. E. Dixon, “Asymptotic Tracking for Systems with Structured and Unstructured Uncertainties,” *IEEE Transactions on Control Systems Technology*, Vol. 16, No. 2, pp. 373-379, (2008).

BIOGRAPHICAL SKETCH

William Scott Bowman was born in St. Petersburg, FL, and spent most of his life there. Growing up, there was not something that had not been taken apart by Scott. He was born an inventor and has always enjoyed working with his hands on mechanical systems. His father provided great guidance to Scott as a young boy always encouraging him to fix it himself.

Scott elected to take three drafting classes and a mechanical design class in high school over the typical PE and “basket-weaving” others took. Scott became an accomplished trumpeter under the private study of Harry Murphy and guidance of Robert Schear. He received several state-level solo performance “superior” ratings and the John Phillip Sousa award for musicianship. Throughout high school he excelled in Math and Science and was involved in a local model aviation club, providing opportunities to experiment early with a variety of small aircraft and robotic systems.

In late June 2001, Scott began attending the University of Florida where he declared an “undecided engineering” major. Scott’s interest in all forms of engineering made it difficult to select a specific study. Scott became involved in 2003 with the Micro Air Vehicles research lab at UF, under the guidance of Dr. Peter Ifju. The lab provided a research opportunity in composite materials, aeronautics and micro electronics. Scott had the unique opportunity to travel abroad for academic competitions with the members of the lab, winning first place on several occasions. In August 2006, Scott received his bachelor’s degree in electrical engineering and won a first place award for his senior design project, titled “MAV Autopilot.”

In January 2007, Scott made the decision to pursue a master’s degree in mechanical engineering with a focus of study on controls and robotics. Scott became very involved with the UF Wildlife and Corps of Engineers UAV programs for the remainder of his graduate school career. Scott graduated in August 2008 with his Master of Science in mechanical engineering.